Chapter II

Electrochemical Assembly of Nickel MOF Decorated Au Dendrites as Peroxidase Mimic for High Performance Hydrogen Peroxide Sensing

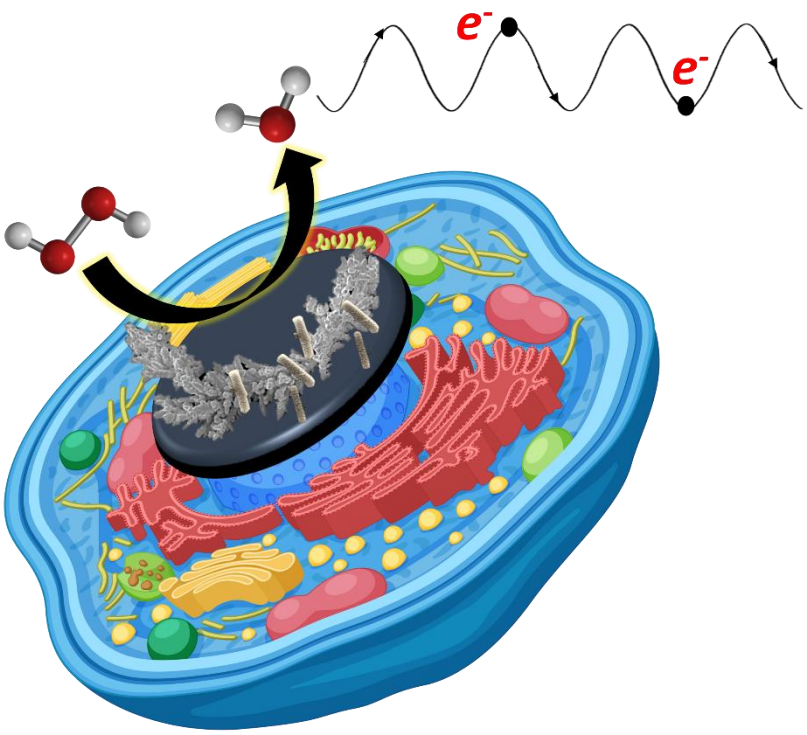

Shubhangi et al., ACS Applied Nano Materials, 2024, 7, 1, 1388–1401.

ACS APPLIED NANO MATERIALS

January 12, 2024
Volume 7
Number 1
pubs.acs.org/acsanm

ACS Chemistry for Life®
AMERICAN CHEMICAL SOCIETY

1. Introduction

H_2O_2, an intermediate in various biological reactions and signalling pathways, is difficult to detect in natural premises due to its instability. However, its excessive concentration can pose threat to cellular health by damaging vital proteins and DNA due to the generation of reactive oxygen species. In view of the importance of H_2O_2 a number of analytical techniques such as colorimetry, fluorescence[1], gas chromatography, high performance liquid chromatography (HPLC)[2], HPLC-UV[3] have been used. Techniques like chromatography and colorimetry are highly skill-dependent ones with necessary preprocessing requirements incurring higher costs and labour for the target specimen detection[4]. Whereas, techniques such as fluorescence can have hindered outcomes due to involvement of interferants. Therefore, to avoid such limitations, electrochemical sensing approach could be a plausible solution due to its rapid response, ease of procedure, sensitivity and low cost[5,6].

Enzymatic sensors are widely being used now-a-days for sensitive and selective sensing of H_2O_2. POD is a naturally occurring enzyme found in many plants as well as few animal cells. This enzyme is known to be highly selective towards combining with H_2O_2 and methyl or ethyl peroxides[7]. Horseradish peroxidase, a heme-containing enzyme of this class, is known to utilize H_2O_2 in order to oxidise vivid variety of organic and inorganic compounds naturally. However, there are significant disadvantages to this century-old enzyme-based sensing technology, including complicated enzyme orientation and controlled immobilization processes, low stability, a compromised shelf life incurring high costs and high response time[8]. To enhance the economic aspect and facilitate a longer lifetime, peroxide sensors in recent years have focussed on the usage of non-enzymatic sensing platforms which have grasped research limelight lately[9–11].

Newer and versatile non-enzymatic sensing platforms with nanohybrid matrices possessing astounding selectivity and stability have been developed recently for H_2O_2 detection[12]. These non-enzymatic systems often aim to overcome the intrusive chemical and thermal instability of enzymatic sensors making their applicability more diverse. However, most of the non-enzymatic sensors require extensive multistep chemical synthesis approaches as the synthesized materials are majorly drop-casted onto the electrode surface[13–15]. Nevertheless, these sensor systems also possess low detection limits and require relatively longer detection time[16]. Thus, a new nanoengineered system can be developed which incorporates the direct deposition of the matrix components in a highly controlled manner onto the electrode surface as a plausible solution.

Metallic dendrites, fern-like 3-dimensional (3D) branched nanomaterials, are known to facilitate electro-oxidation and electro-reduction of analytes by virtue of the metallic species present in them, such as palladium (Pd), platinum (Pt), silver (Ag), gold (Au) etc.[17,18]. Furthermore, the branching structure offers a significant number of electroactive sites facilitating electron transfer and thereby conductivity. Another class of materials gaining prominence lately is Metal Organic Framework (MOF). These microporous structures are made up of coordinated metal clusters and organic ligands which when incorporated in electrochemical systems impart them with unique properties such as high surface to volume ratio, large pore sizes, surface tunability, and functional potential[12]. However, their properties are often compromised by low conductivity and catalytic properties when compared to classic metallic structures due to the presence of organic linker moieties in their framework resulting into electrode fouling[19,20]. Much reports on their application in sensor matrices' component have discussed their synthesis through the solvothermal route[21,22]. There have been recent reports on MOF-based non-enzymatic H_2O_2 sensors which have highlighted MOFs to be suitable sensor matrix component,

however, such sensors are dramatically compromised due to micromolar range of detection which does not comply with clinical range of the analyte[23]. It is very well established that in heterogeneous biological systems the H_2O_2 concentration window lies in sub-nanomolar ranges[24]. Since the outflux of H_2O_2 from cellular microenvironment is dynamic in most of the biological fluids, the detection time should be as low as possible in such complex cellular matrices. Therefore, the sensor should be crafted with desirable traits encompassing all critical features including (i) low detection time, (ii) less contact time with biological fluid to avoid fouling effect, (iii) sub-nanomolar analysis with wide dynamic detection range, and (iv) ease of fabrication. Furthermore, the limiting feature of MOFs in terms of the conductivity can be improved through its systematic fabrication via the electrochemical route[25], as an attractive alternative to cope up with its limitations and facilitate lower detection ranges. Considering the uniqueness of metallic dendrites and MOF-based matrices, we hypothesize that a nanohybrid material comprising these can be an interesting combination that can show remarkable performance as a sensor matrix for rapid detection of clinically relevant molecules such as H_2O_2.

In view of this, an innovative nanohybrid sensor matrix has been designed. A controlled electrodeposition process was adopted for nanoimprinting the AuND over the glassy carbon electrode (GCE) surface. Then, electrochemical deposition of Ni-MOF has been done to improve surface area to many folds. The surface has been further modified by adding a thin coat of hydrazine, which is considered as a powerful electrocatalyst for electrochemical reduction of H_2O_2[26]. The nanohybrid sensing matrix, GCE/AuND/Ni-MOF/Hyd exhibited commendable electrical and catalytic properties and was finally redirected towards the non-enzymatic detection of H_2O_2. Each layer was characterized using various physical and electrochemical techniques to establish its complete morphology and physico-chemical characteristics. The sensor surface was vigorously studied for its conductive and catalytic

behaviour through a series of electrochemical analyses such as, CV, EIS, linear sweep voltammetry (LSV), and chronoamperometry (CA). The analytical strength of the developed sensing probe to detect H_2O_2 was assessed using the LOD and LDR studies. The applicability of the nanohybrid sensing probe for H_2O_2 detection was validated in synthetic serum samples. The efficacy and selectivity of the sensor towards H_2O_2 through study involving co-existing molecules was also investigated. Reproducibility of results on different electrodes' surfaces over a period of time was checked as well. To the best our knowledge, this fabricated nanohybrid system is the first sensing module comprising of AuNDs intercalated with MOFs, thereby generating enormous surface area, has been developed for high performance H_2O_2 sensing. The stages of sensor fabrication and the H_2O_2 detection strategy has been illustrated in **Figure 2.1.**

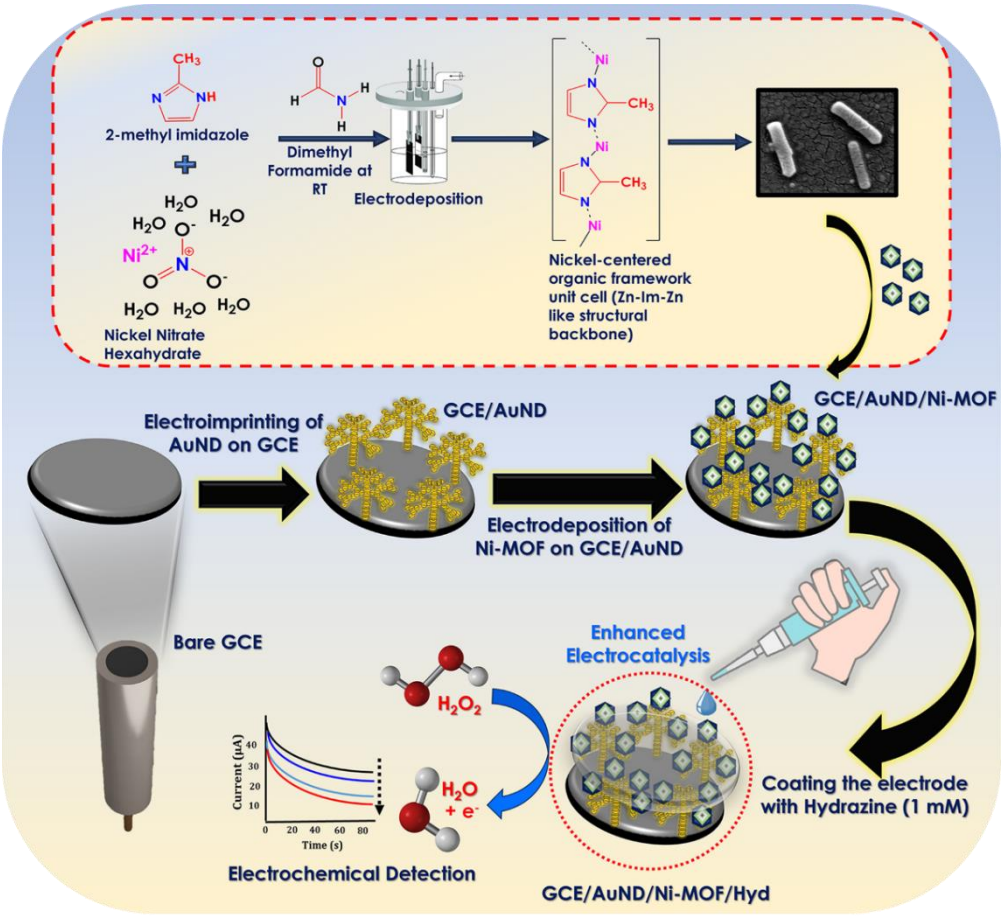

Figure 2.1. *The upper panel discusses the structural assembly of Ni-MOF components whereas the lower panel gives an overall detailed diagrammatic representation of the development of nanohybrid sensing probe for electrocatalytic detection of H_2O_2.*

2. Materials and Methods

2.1. Chemicals and Instruments

All reagents and chemicals used in the current experimental setup were of analytical grade. Potassium hexacyanoferrate (II) ($K_4Fe(CN)_6$) and potassium hexacyanoferrate (III) ($K_3Fe(CN)_6$) were procured from Himedia Pvt. Ltd, Mumbai, India. Nickel nitrate hexahydrate ($Ni(NO_3)_2.6H_2O$), 2-methyl imidazole (2-MeIm), dimethyl formamide (DMF), sodium monophosphate (NaH_2PO_4), sodium bisphosphate (Na_2HPO_4), potassium chloride (KCl), chloroauric acid ($HAuCl_4.3H_2O$) were bought by Sisco Research Pvt. Ltd, Delhi, India. Hydrogen Peroxide (H_2O_2) was obtained from Sigma-Aldrich Chemical Co. (India). Double-distilled water from a Milli-Q water purifier (water resistance 18.2 MΩ) was used for the preparation of standard solutions. Physical characterizations were carried out on a set of instruments facilitated by the Central Instrument Facility Centre (CIFC) IIT (BHU) such as the XPS [Thermo Fisher K-Alpha instrument], SPM, SEM [FEI Quanta 200 FEG instrument], FTIR [Nicolet iS5, Thermo Electron Scientific Instruments LLC], XRD [Rigaku Miniflex 600 Desktop X-Ray Diffraction System]. An electrochemical analyser (Palm Sense 4.0) comprising of a three-electrode system with GCE as the working electrode and platinum wire, and silver/silver chloride (Ag/AgCl) as auxiliary, and reference electrodes, respectively. The system was used to evaluate the electrochemical characteristics of the nanohybrid sensing probe and thereafter, its analytical efficiency.

2.2. Preparation of GCE/AuND/Ni-MOF/Hyd sensing probe

Initially, the bare GCE electrode surface was polished with the alumina slurry (0.5 micron) and then, was thoroughly rinsed with double-distilled water to wash away all impurities. The first step involved electro-imprinting the AuND over the GCE surface for

which 10 mM $HAuCl_4.3H_2O$ was dissolved in 0.1 M KCl solution and thereafter optimally electrodeposited at -0.30 V vs. Ag/AgCl for 1500 seconds. Further, Ni-MOF was deposited onto the surface of the dendrite by dissolution of 50 mM $Ni(NO_3)_2.6H_2O$ and 75 mM of 2-MeIm in 10 ml DMF solvent system at -1.4 V vs. Ag/AgCl for 300 seconds in optimized conditions systematically. The GCE/AuND/Ni-MOF probe was further modified by coating it with 1mM hydrazine prepared in phosphate buffer saline (PBS) to form the final layer as GCE/AuND/Ni-MOF/Hyd post incubation for 20 minutes. Different sets of electrochemistry-based control experiments were conducted to validate the presence of metal ions and hydrazine in a 0.5M sulphuric acid (H_2SO_4), 0.1M NaOH, and 0.1M PBS in vivid experimental settings. In this, each layer of the nanoengineered probe surface was separately developed and thoroughly characterized for comparative evaluation critically. The final probe was washed with double-distilled water and ethanol sequentially and dried and kept in desiccator for further usage.

Testing process of H_2O_2 involved an initial electrode scanning in 0.1 M PBS buffer solution (blank) with no H_2O_2 present in it. In the next step, H_2O_2 was added in the solution with increasing concentrations (0.1 to 0.5 M H_2O_2), in a three-electrode system setup. This control study was followed by testing the developed probe further at low concentrations of H_2O_2 (10^{-8} to 10^{-15} M H_2O_2) to obtain the calibration plot. The overall reaction of electroreduction of H_2O_2, aided by hydrazine, can be understood through **Figure 2.1.**

2.3. Electrochemical characterizations of the GCE/AuND/Ni-MOF/Hyd nanohybrid sensing probe

The Zobbles electrolytic solution (ZS) ($K_3[Fe(CN)_6]/K_4[Fe(CN)_6]$), 5mM; pH-7) was used to carry out the electrochemical characterizations of the GCE/AuND/Ni-MOF/Hyd nanohybrid surface through techniques such as CV and EIS. The EIS data was recorded

at a rate of ten points per decade sampling, with an open circuit voltage in the analysis range of 10 to 10^4 Hz. Further, the amperometric responses were logged upto 80 seconds at potential and equilibration time of -0.4 V vs. Ag/AgCl and 10 seconds, respectively, to acquire the standard calibration plot of H_2O_2.

2.4. Real Sample Analysis

The real-life application of the developed nanohybrid sensing probe GCE/AuND/Ni-MOF/Hyd was validated on synthetic serum samples. For the effective validation study on detection of H_2O_2, a conventional spike and recovery model was used. The synthetic serum was equilibrated with PBS by 10 times dilution and then spiked with varying concentrations of H_2O_2. This is a vital step to maintain the molar strength of the real matrix when compared with the standards to prove the sensor's performance. The recorded output current was plotted and compared with the calibration curve obtained from an initial concentration-dependent study on H_2O_2 in standard buffer solutions.

3. Results and Discussion

3.1. Electrochemical nanoimprinting and characterization of 3D AuND/Ni-MOF/Hyd nanohybrid sensing probe

An optimized synthesis of AuND was done through a simple yet robust electroimprinting technique was followed by Ni-MOF electrodeposition followed by functionalization with a thin layer of Hyd. The electrochemically nanoimprinted **AuND/Ni-MOF/Hyd** probe was thoroughly characterized physically as well as electrochemically to validate its formation. Various physical techniques were adopted at first stage to confirm the probe deposition of MOF layer.

3.1.1. SPM studies

At the first stage, SPM was conducted for each layer of the sensor probe. The electrode was thoroughly cleaned and imprinted with AuND and utilized for the study. In further samples, the Ni-MOF and hydrazine were layered and grown onto the electrode surface and were scanned respectively in tapping mode. The probe and cantilever specifications have been detailed under heading '**Additional information**' in the adjoining box.

Additional Information: Details on the SPM Cantilever Specifications

Model: NTEGRA Prima; **Company:** NT-MDT Service & Logistics Ltd.

Characterization was performed through a Noncontact Polysilicone probe, tip material comprised of silicon with cantilever chip size being 1.6 x 3.6 mm and thickness of 0.45 mm. The curvature radius of the tip was around 10 mm. The cantilever specifications were as follows:

- Cantilever length (in µm): 94 with a typical dispersion of about ± 2
- Cantilever width (in µm): 34 with a typical dispersion of about ± 3
- Cantilever thickness (in µm): 1,85 with a typical dispersion of about ± 0.15
- Force Constant (N/m) = 12 with a typical dispersion of about ± 20%
- Resonant Frequency (kHz) = 235 with a typical dispersion of ± 10%

The bare surface shows an evenly distributed pattern throughout the pitch of analysis (**Figure 2.2A and 2.2a**). Upon deposition of nanodendrite, enlarged crests of relatively bigger size with significant changes in the surface topology can be seen. A uniform distribution of crests was seen throughout the analysis window suggesting even surface fabrication (**Figure 2.2B and 2.2b**). After this step, on electrodeposition of Ni-MOF, the surface topological characteristics change drastically with additional bigger crests visible which could be due to the successful formation of the MOF, embedded on dendritic surface (**Figure 2.2C and 2.2c)**. In the last step, when the hydrazine was coated onto the final probe, a highly patterned surface topology was

observed which was completely different from the previous ones, as seen in **Figure 2.2D and 2.2d**, thereby concluding the steps to final probe fabrication. The SPM analysis was also numerically evaluated through scrutiny of SPM parameter such as z-deflection values, where the incremental shift in values was observed with increase in successive layers on the sensor probe. The z-deflection values obtained at various magnifications establish the uniformity of materials formed through the electrodeposition of layers on the electrode surface. The SPM results can be better understood through values stated in **Figure 2.2,** where a gradual increase in the z-deflection on successive layer deposition is an indicative of successful uniform probe surface fabrication. Since in this study there are defined patterned structures, whose morphology remain uncertain, SEM, EDX and FTIR analyses were taken into consideration for affirmation of structural morphology and chemical insights.

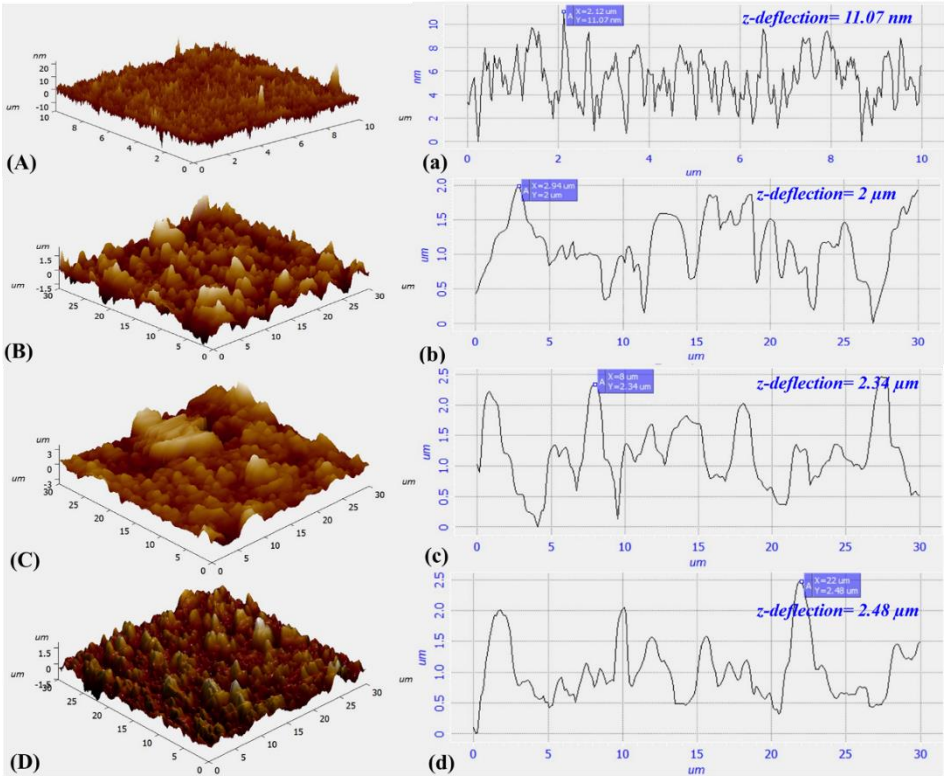

Figure 2.2. ***(A)*** *SPM 3D and its respective 2D graph (a) illustrating surface of the bare electrode;* ***(B)*** *SPM 3D and SPM 2D (b) graphs corresponding to the second layer of electrode/AuND;* ***(C)*** *SPM 3D and its corresponding SPM 2D graph(c) for the third layer, i.e., electrode/AuND/Ni-MOF; and* ***(D)*** *SPM 3D and SPM 2D graph(d) demonstrating the distinctly developed crests and uniform surface distribution of Hyd.*

3.1.2. Physical characterization of sensing probe/ probe materials

SEM analysis was conducted to thoroughly investigate the nanostructural morphology. A clean electrode surface was taken to nanoimprint AuND onto it followed by subsequent modification with Ni-MOF to obtain AuND/Ni-MOF probe surface. **Figure 2.3A** depicts the nanodendritic imprint intercalated with Ni-MOF. A uniformly distributed fern-like forest of Au dendrites flanked with similar structures possessing distinct primary (1°), secondary (2°) and tertiary (3°) branches (specified through orange and red dotted lines) were observed, as shown in **Figure 2.3B and 2.3C** (zoomed image of GCE/AuND/Ni-MOF). The 1° branches were seen bifurcating into smaller 2° branches and then into thinner 3° branches, as evident from the images. Ni-MOF nanostructures as a component of AuND/Ni-MOF hybrid was seen clearly intercalated with the dendritic structures (as encircled in blue color in the **Figure 2.3B and 2.3C**). To establish the firm belief on the presence of AuND and Ni-MOFs, both the components were exclusively electrodeposited on a bare electrode surface too. This separate study confirmed the leaf-like morphology of AuNDs as well as the rod-like morphology of Ni-MOFs, as seen in the imaged area (**Figure 2.3D and 2.3E**). The zoomed-in view of the Ni-MOF can be clearly seen in **Figure 2.3F**.

Further, to validate the elemental composition of the AuND/Ni-MOF nanohybrid, elemental mapping coupled with EDX analysis was carried out. The mapped results shown in **Figure 2.4A** demonstrates the merged micrograph of all elements viz. Au (**Figure 2.4A-I**), Ni (**Figure 2.4A-II**), N (**Figure 2.4A-III**) and C (**Figure 2.4A-IV**) illustrated through **orange, cyan, dark green,** and **olive green-colored** patterns**,** respectively. For better clarity the merged micrograph segregated into constituent element micrographs has been depicted in **Figure 2.4A (I-IV)**. EDX analysis confirms the presence of Au, Ni, N, and C elements in the atomic percentage of about 31.3%, 5.4%,

20.0 %, and 25.2 %, respectively **(Figure 2.4B)**. With these atomic proportions, we postulated a structure of the Ni-MOF (as illustrated in **Figure 2.1**) which as a framework should look morphologically identical to Zn-Im-Zn like-arrangement seen in ZIFs. The metal center 'Ni' is postulated to be attached to two imidazole linker moieties through the pyrrolic 'N' lone pairs which makes the ratio look like $[C_4H_6N_2]_2$ connected to one 'Ni' metal center. This makes the ratio of N:Ni as 4:1 which exactly matches with the EDX atomic percentage ratio for N:Ni, forming a 2D framework. Hence, it is possible to infer that Ni-MOF is being formed. Also, the C 1s percentage of the elucidated characterization shows greater atomic percentage of C 1s than the N 1s which is as obvious by their presence in the imidazolate structure where C 1s is in excess. After the confirmatory tests for deducing the elemental composition of the constituents present in the sensor matrix, XRD and FTIR spectra was also obtained to reconfirm the crystalline nature, phase formation and functional groups of the Ni-MOF **(Figure 2.5).** The FTIR spectrum for Ni-MOF was obtained at a wavenumber scope of 4000-450 cm^{-1} to understand the functional groups present in the structure. The spectrum exhibits various peaks corresponding to the bending and stretching vibrations of the imidazole linker ring in the region of 450-1500 cm^{-1} and are comparable to those reported in previous literature[27]. The FTIR spectrum presented with peaks corresponding to desirable functional groups confirming the successful synthesis of Ni-MOF through the novel route (**Figure 2.5A**). The -OH stretching vibration at 3450 cm^{-1} corresponds to the moisture as well as hydroxyl moieties present in the MOF structure. Two peaks located at 2929 and 3135 cm^{-1} correspond to =C-H bond vibrations from the aromatic and aliphatic rings in the imidazole structure. In addition to this, two doublet peaks were also observed at 679 and 740 cm^{-1} belonging to the C-H stretching bonds present in the methyl group of the linker. A classic peak at around 472 cm^{-1} corresponds to Ni-N bond which establishes the notion for successful

Ni-MOF formation[27]. Apart from this, the alkene C=C group in the linker contributes to a peak at around 1650 cm^{-1}. Furthermore, in the XRD analysis, the strong diffraction peak at around 14° distinctly confirmed the crystalline structure of the electrodeposited Ni-MOF **(Figure 2.5B)** which is consistent with the previously reported literature[28].

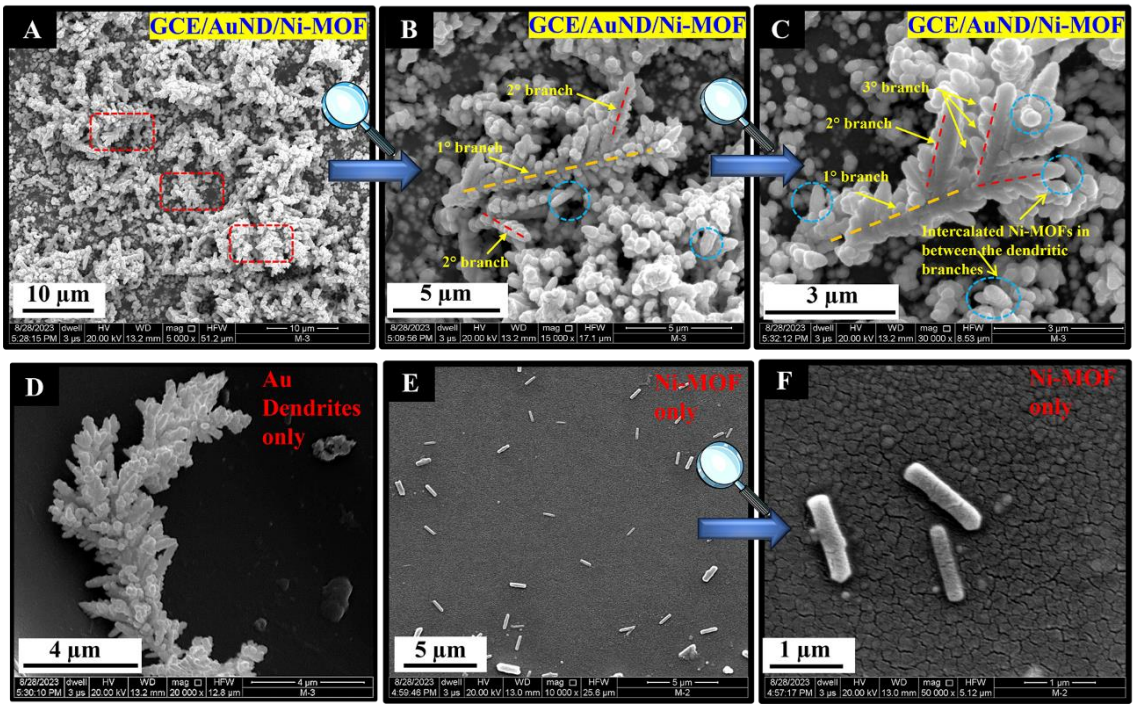

Figure 2.3. ***(A)*** *depicts the SEM image of AuNDs (red square) intercalated with Ni-MOF at a scale of 10 µm;* ***(B)*** *and* ***(C)*** *shows zoomed-in SEM micrographs of Ni-MOFs grown over the surface of metallic dendrites (blue circle) at 5 and 3 µm scale, respectively, a distinct fern like architecture of AuNDs with 1°, 2° and 3° branching was seen;* ***(D)*** *shows zoomed-in Au dendrites* ***(E)*** *illustrates uniform distribution of rod-like Ni-MOFs at 5 µm and* ***(F)*** *zoomed-in image of the Ni-MOFs at 1 µm scales, respectively.*

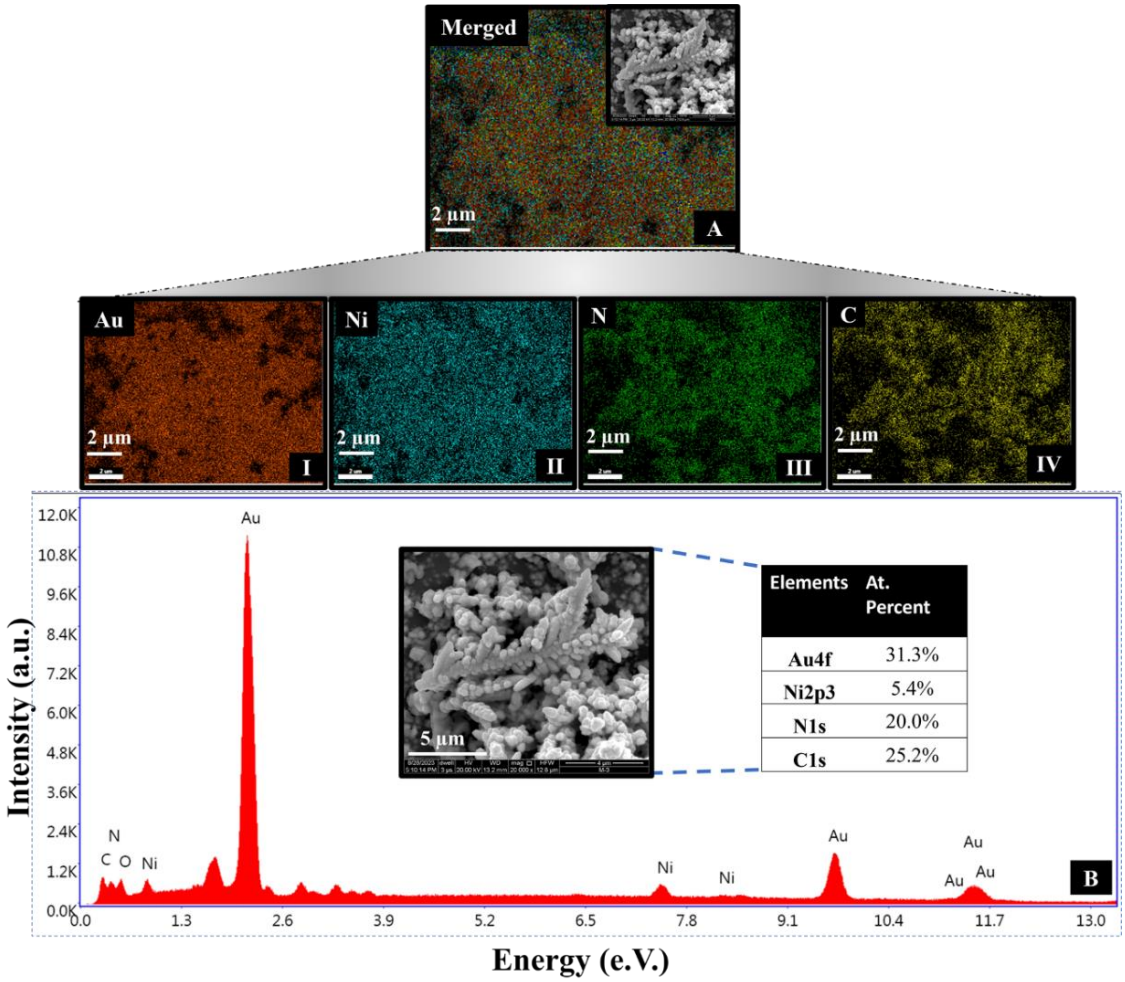

Figure 2.4. ***(A)*** *depicts the merged elemental mapping of AuND/Ni-MOF probe, showing the distribution of all the elements, viz. Au* ***(orange),*** *Ni* ***(cyan),*** *N* ***(dark green),*** *and C* ***(olive green color)*** *over its surface. The micrograph of individual elements is also depicted separately in* ***2.4A (I-IV)****;* ***(B)*** *EDX analysis of AuND/Ni-MOF probe confirming the presence of constituent elements, Au* ***(orange),*** *Ni* ***(cyan),*** *N* ***(dark green),*** *and C* ***(olive green color)*** *with their respective atomic percentage in the nanostructure, as depicted in the adjoining table.*

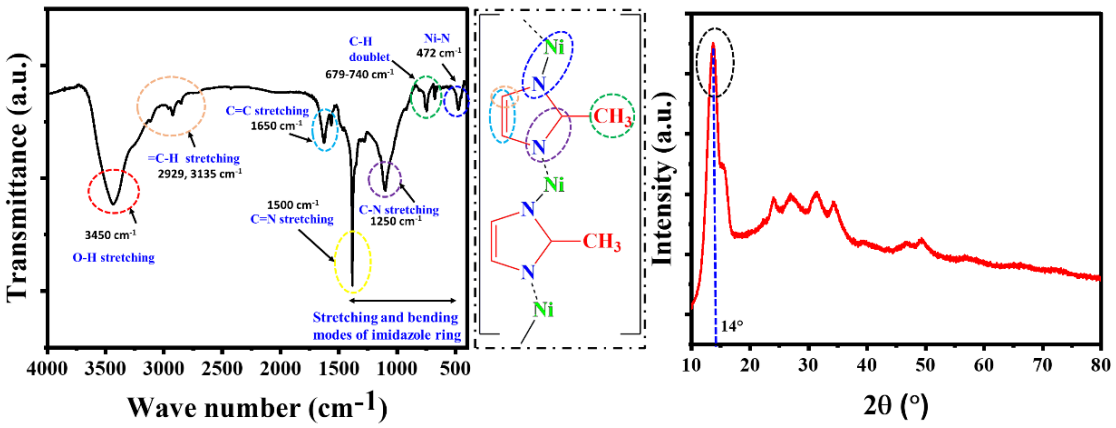

Figure 2.5. ***(A)*** *FTIR and* ***(B)*** *XRD spectra corresponding to the fabricated Ni-MOF.*

These studies are suggestive of the successful coating of different layers at the electrode surface, however, to further dig into the chemical functionalities and oxidation states of all constitutive elements in the developed probe, XPS analysis was performed.

3.1.3. XPS analysis

To validate the elemental composition and the metal oxidation states on the fabricated surface, the sensor probe underwent XPS examination. XPS spectra of Au 4f, Ni 2p, C1s, and N1s elements in the dendrites, MOF and hydrazine components presence on the electrode surface, GCE/AuND/Ni-MOF/Hyd are depicted in **Figure 2.6A, 2.6B, 2.6C, and 2.6D**. The highly resolved XPS spectrum of Au 4f reveals two doublet peaks at 83.66 and 87.48 e.V. **(Figure 2.6A (i) a,b)** which on deconvolution corresponds to characteristic peaks of metallic Au^0 on the GCE/AuND surface[29]. These peaks are present in case of GCE/AuND/Ni-MOF/Hyd surface as well **(Figure 2.6A (ii) a,b)** however, their intensity slightly diminishes. This was most likely due to the fabrication of successive layers, confirming their successful coating. The deconvoluted XPS spectra of Ni shows four distinct peaks **(Figure 2.6B (ii) a-d),** for the GCE/AuND/Ni-MOF/Hyd surface, which were not observed earlier in the case of GCE/AuND surface, **(Figure 2.6B (i))** indicating that the peaks in the former correspond to Ni-MOF only. Of all visible peaks of the spectrum, peaks 'a' and 'c' correspond to $Ni(2p_{3/2})$ and $Ni(2p_{1/2})$ core levels while 'b' and 'd' represent their corresponding shakeup satellite peaks (sat.), respectively. The peaks located at binding energy values of 855.08, 860.61, 872.58, and 879.09 e.V. can be designated to $Ni^{2+}(2p_{3/2})$, $Ni^{2+}(2p_{3/2})$ shakeup satellite, $Ni^{2+}(2p_{1/2})$, and $Ni^{2+}(2p_{1/2})$ shakeup satellite peaks, respectively[30,28]. The intense peaks corresponding to $Ni^{2+}(2p_{3/2})$ and $Ni^{2+}(2p_{1/2})$ establish the presence of Ni core levels in its Ni^{+2} state within the MOF when bonded to imidazole linker moiety. The hypothesized structure in **Scheme 1** also indicates the Ni metal center to exist as Ni^{+2}. The difference between the core level Ni

peaks (17.5 e.V.) and the satellite peaks (18.48 e.V.) remained comparable[30,31]. Further, the sample was examined for the presence of C 1s **(Figure 2.6C (a,b))** and N 1s (**Figure 5D**) peaks. The peaks at 284.18 e.V. and 287.69 e.V. correspond to C=C and C-N bonds, respectively, which are testament for the presence of these elements in the imidazole backbone of the Ni-MOF, as shown in **(Figure 2.6C (ii) a,b).** These representative peaks, however, were absent when GCE/AuND was examined verifying that the peaks are merely due to the successful coating of Ni-MOF onto the electrode surface**.** Further, on consideration of the N 1s spectrum, a distinct peak was observed at binding energy value of 398.38 e.V. for GCE/AuND/Ni-MOF and GCE/AuND/Ni-MOF/Hyd as shown in **(Figure 2.6D (ii and iii)),** respectively, confirming the presence of C-N bond which complements with the results of the C 1s spectrum[28,32]. These peaks signify the imidazole linker moieties of the framework which were absent in case of GCE/AuND **(Figure 2.6D (i)),** suggesting that these peaks are due to the elements of the imidazole framework, exclusively. The N 1s peak intensifies on the addition of hydrazine layer onto the electrode surface in the final step of the GCE/AuND/Ni-MOF/Hyd probe fabrication. The detailed XPS spectra and thereby increment in atomic N1s percentage has been provided in **Figure 2.7** and **Figure 2.8**. XPS analyses, thus, evidenced the presence of both metals as well as non-metals in their desired states on the nanoimprinted surface.

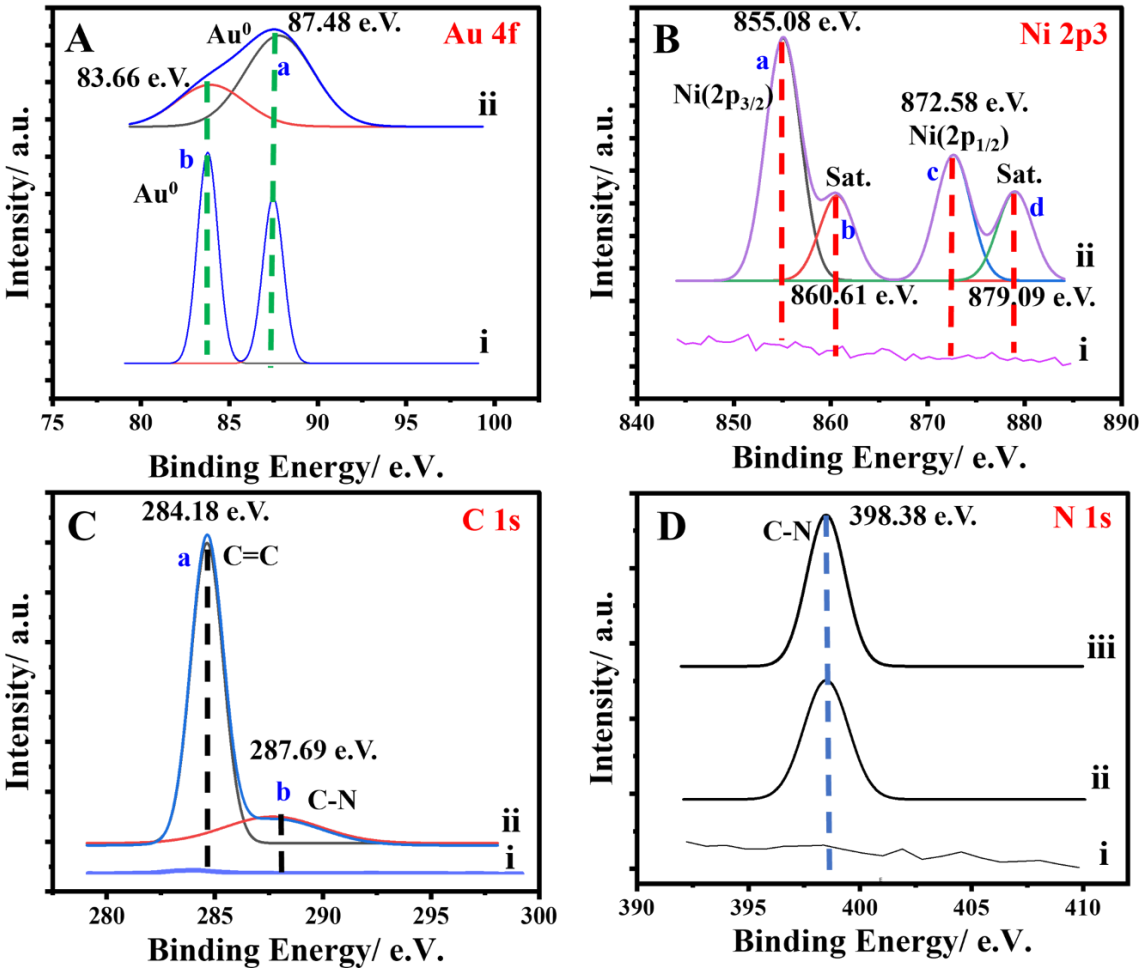

Figure 2.6. *XPS spectra stating the oxidation states of elements present in the sensor matrix.* ***(A)*** *XPS spectrum corresponding to Au^0 (i)GCE/AuND and (ii)GCE/AuND/Ni-MOF/Hyd probe surfaces;* ***(B)*** *XPS spectrum of Ni element (i) for GCE/AuND and (ii) GCE/AuND/Ni-MOF/Hyd surfaces can be deduced into 4 peaks. Absence of these peaks in (i) represent the absence of Ni in GCE/AuND surface.* ***(C)*** *represents the XPS spectrum of C 1s (i) in GCE/AuND surface and (ii) GCE/AuND/Ni-MOF/Hyd final probe surface.* ***D)****XPS spectra for (i) GCE/AuND (ii) GCE/AuND/Ni-MOF and (iii) GCE/AuND/Ni-MOF/Hyd surfaces.*

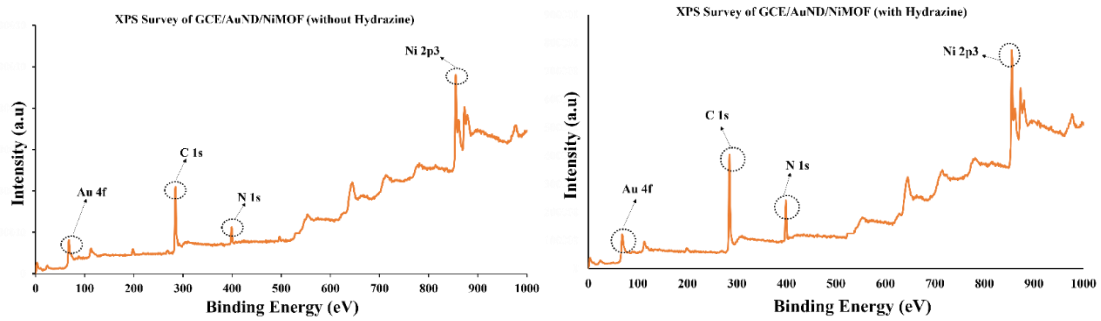

Figure 2.7. *A comparison for the XPS spectra of GCE/AuND/Ni-MOF surface wihout and with the presence of hydrazine. An enhancement in the peak corresponding to N 1s was seen by upto 5 atomic % clearly stating the successful functionalization of probe surface with hydrazine in the final step.*

Elements	Atomic Percentage (GCE/AuND/Ni-MOF)	Atomic Percentage (GCE/AuND/Ni-MOF/Hyd)
Au4f	0.05%	0.01%
Ni2p3	12.02%	11.04%
N1s	7.33%	12.46%
C1s	46.5%	50.22%

Figure 2.8. *A comparative atomic percentage of GCE/AuND/Ni-MOF and GCE/AuND/Ni-MOF/Hyd. With an introduction of Hyd, there appears an enhancement in N 1s peak implying successful coating of Hyd on the probe surface.*

The physical characterisation results were verified through a series of electrochemical experiments as discussed in further sections below.

3.1.4. Validation of Au, Ni, and hydrazine presence at the electrode surface

The presence of Au, Ni, and Hyd in the sensing matrix was systematically examined through a series of experiments with various controls.

The fabricated GCE/AuND/Ni-MOF/Hyd probe was scanned in the potential window of +0.5 V to +1.5 V vs. Ag/AgCl in 0.5 M H_2SO_4 solution. In this case, the representative Au redox peaks were observed at +1.20 (**a**) and +0.98 V (**b**) vs. Ag/AgCl (as depicted in **Figure 2.9, black curve**) which are testimony of the presence of Au in the final fabricated probe surface[33,34]. This was further verified by a negative control experiment where bare GCE was tested in the similar experimental conditions where no redox peaks were observed (**Figure 2.9**, **green curve**). The elemental validation was done for Ni, where, the GCE/AuND/Ni-MOF/Hyd probe was tested in a solution of 0.1 M NaOH by scanning the potential between -0.5 V to +0.3 V vs. Ag/AgCl. Sharp anodic and cathodic peaks corresponding to Ni were observed at +0.20 V (**c**) and -0.20 V (**d**) vs. Ag/AgCl (**Figure 2.9, blue curve**). Similar scan results in bare GCE yielded no peaks at these corresponding potential values signifying the peaks to be exclusively belonging to

elemental Ni[35] (**Figure 2.9**, **brown curve**). In another set of control studies, the GCE/AuND/Ni-MOF/Hyd probe was subjected to 0.1 M PBS and scanned within a potential range of -1.0 V to +0.1 V vs. Ag/AgCl. A sharp anodic peak was observed at -0.20 V (**e**) vs. Ag/AgCl which confirmed the presence of adsorbed hydrazine on probe surface (**Figure 2.9, red curve**). In its negative control counterpart, no peak was seen in case of bare GCE (**Figure 2.9, pink curve**) stating the peak in the former study to be corresponding to hydrazine only[26]. It was followed by validation of electron transfer mechanism and stability of Au, Ni, and Hyd through a scan rate dependent analysis of final nanohybrid sensing probe in 0.5 M H_2SO_4, 0.1 M NaOH, and 0.1 M PBS solutions, respectively. Cathodic (Ipc) and anodic (Ipa) peak currents were found to be directly proportional to the scan rates with correlation coefficient values corresponding to 0.99 and 0.99 for Au (**Figure 2.9A**), 0.99 and 0.95 **(Figure 2.9B)** for Ni, and 0.88 for hydrazine (**Figure 2.9C)**, respectively. These set of experiments successfully confirm the presence of Au, Ni metals and hyd on the developed sensor probe. Along with it, these findings evidently demonstrate that electron transport was taking place primarily aided by surface adsorption phenomenon occurring at the sensor surface. It also evidents the stability of the probe surface even at higher scan rates[36],making it an ideal engineered surafce for real sample examination.

These outcomes clearly show that the sensor surface underwent adsorption processes and is extremely stable, even at higher scan rates.

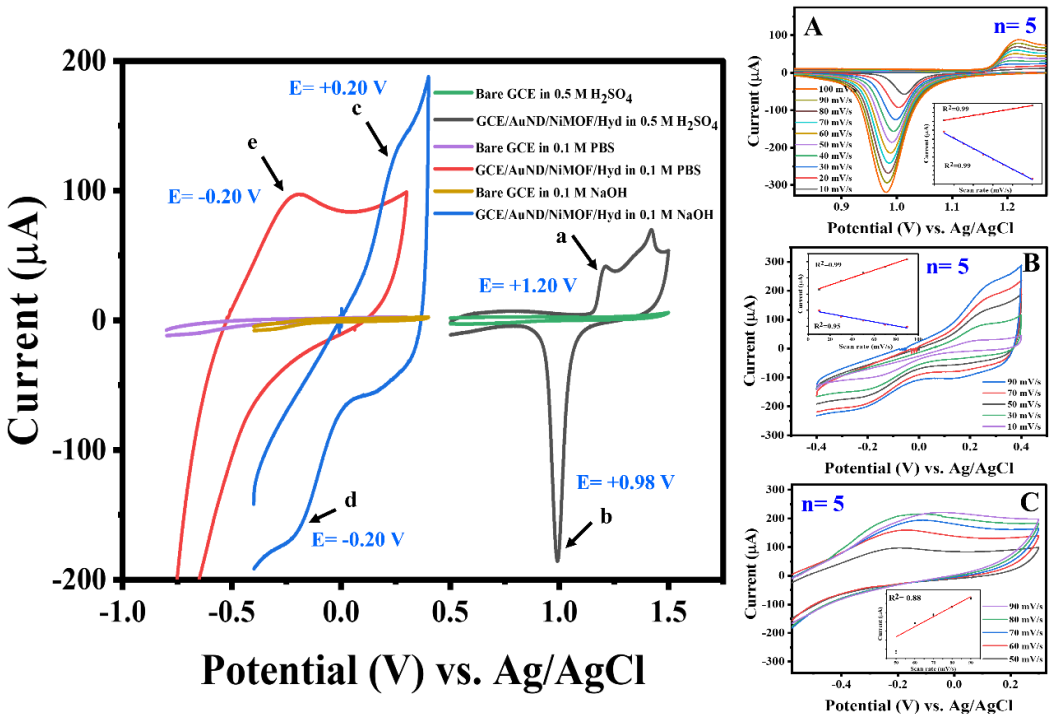

Figure 2.9. *CV curve of bare GCE and GCE/AuND/Ni-MOF/Hyd surfaces in 0.5 M H_2SO_4* ***(black curve)****, 0.1 M NaOH* ***(blue curve)****, and 0.1 M PBS* ***(red curve)****.* ***(A)*** *Scan rate analysis of GCE/AuND/Ni-MOF/Hyd probe in 0.5 M H_2SO_4 with a scan rate varying between 10-100 mV/s; inset representing the linearity between the current and scan rate,* ***(B)*** *Scan rate analysis of GCE/AuND/Ni-MOF/Hyd probe in 0.1 M NaOH with the scan rate varying from 10 to 100 mV/s; inset representing the linearity between the current and scan rate,* ***(C)*** *Scan rate analysis of GCE/AuND/Ni-MOF/Hyd probe in 0.1 M PBS; inset shows corresponding peak values showed linearity. Here, n=5 denotes the number of iterations performed.*

3.1.5. Electrochemical characterization of GCE/AuND/Ni-MOF/Hyd sensing probe

Post verifying the presence of desirable sensing probe elements such as Au, Ni metals and Hyd, the fabricated GCE/AuND/Ni-MOF/Hyd probe was proceeded for electrochemical examination to examine its conductive and electrocatalytic properties. CV was conducted in 5 mM ZS at a scan rate of 50 mV/s in an analysis window of 0 to +1.0 V vs. Ag/AgCl (n=5) (**Figure 2.10A)**. Peaks within a potential window of +0.2 to +0.8 V vs. Ag/AgCl were observed due to the inherent redox behavior of ZS at GCE **(red curve)**.

Peaks referring to GCE/Ni-MOF (**blue curve),** GCE/AuND (**pink curve**), GCE/AuND/Ni-MOF (**green curve**) and GCE/AuND/Ni-MOF/Hyd electrode (**black curve**), have been illustrated in **Figure 2.10**. MOFs have always been known to hamper

the conductivity of the sensor probe but in our case, interestingly, when the GCE surface was electrochemically deposited with Ni-MOF, a rise in conductivity was noted. Such electrodeposited MOF-dependent conductivity enhancement has been also observed earlier for different MOFs[37]. Apart from that, bare GCE when electrodeposited with AuND also exhibited a rise in conductivity. On hybridizing the surface of the GCE with AuND and Ni-MOF sequentially, led to a humongous rise in conductivity (**green curve**). This unexpected rise is an interesting result where we were successfully able to develop a hybrid module comprising of a novel combination of AuND and Ni-MOF for the very first time. A comparative histogram was plotted to understand the redox current response of each layer of the electrode **(Figure 2.10B).** The current density was elevated with addition of Ni-MOF and AuND with the maximum current density observed for GCE/AuND/Ni-MOF, attributed to the synergistic impact of highly conductive surface embedding the conductive MOF components. It was statistically analyzed through a t-test calculation and the p-value was found to be < 0.03.

The numerical quantification of each surface's electrocatalytic activities and charge transfer characteristics was done through the estimation of the effective surface area (A) using the Randles-Sevcik's equation [38,39]

$$I_p = \left(2.69\times10^5\right) n^{3/2}\, ACD^{1/2}\, v^{1/2} \quad \text{…Equation i}$$

where, Ip stands for the highest current output (in amperes), n is the no. of electrons involved in redox reaction (here n = 1), A implies the electrodes' effective surface area (in cm^2), C represents the electroactive species' concentration (in mole cm^{-3}), D denotes the diffusion coefficient (in $cm^2\ s^{-1}$) and its value is 7.6 × 10^{-6} cm^2s^{-1} for aqueous ferrocyanide, and v is the scan rate (in Vs^{-1}).

The active surface area of GCE, GCE/Ni-MOF, GCE/AuND, GCE/AuND/Ni-MOF, and GCE/AuND/Ni-MOF/Hyd was calculated as 70.11 × 10^{-3} cm^2, 97.17 × 10^{-3} cm^2, 150.06 × 10^{-3} cm^2, 432.96 × 10^{-3} cm^2, 291.57 × 10^{-3} cm^2. As lucid these area results are, they clearly emphasize our established notion so far where the conductivity rise is consistent with addition of subsequent layers on the GCE surface. The area statistics for the GCE/AuND/Ni-MOF nanohybrid sensing probe reveal a rise in about 6.18, 4.46, 2.88 and 1.48 times, when compared to bare GCE, GCE/Ni-MOF, GCE/AuND, and GCE/AuND/Ni-MOF/Hyd, respectively. This backs the higher conductivity and electron transfer capabilities of the designed nanohybrid sensing probe. The conductivity on addition of hydrazine decreases slightly due to presence of organic moieties in it **(black curve).** However, its presence is quintessential for the effective sensing of our target analyte H_2O_2 through reduction.

The validation of CV output was complimented through EIS experiment **(Figure 2.10C).** The values obtained by circuit fitting for GCE **(red curve)**, GCE/Ni-MOF **(blue curve),** GCE/AuND **(pink curve),** GCE/AuND/Ni-MOF **(green curve)** and GCE/AuND/Ni-MOF/Hyd electrode surfaces **(black curve)** were plotted as their respective Nyquist plots. The corresponding Rct values were determined through the respective Nyquist plots pertaining to each probe surface viz., 6542 (±102.12) Ω, 4585 (±101.49) Ω, 2375 (±103.55) Ω, 251 (±103.55) Ω, and 409 (±108.51) Ω, respectively. There was a gradual decline in the charge transfer resistance with each fabrication step upto GCE/AuND/Ni-MOF layer. A slight increase the resistance of the GCE/AuND/Ni-MOF/hyd was observed complimenting the CV results. The overall EIS findings are in good agreement to the CV analysis **(Figure 2.10D)**. This makes it a suitable matrix for the electrochemical sensing of our target analyte.

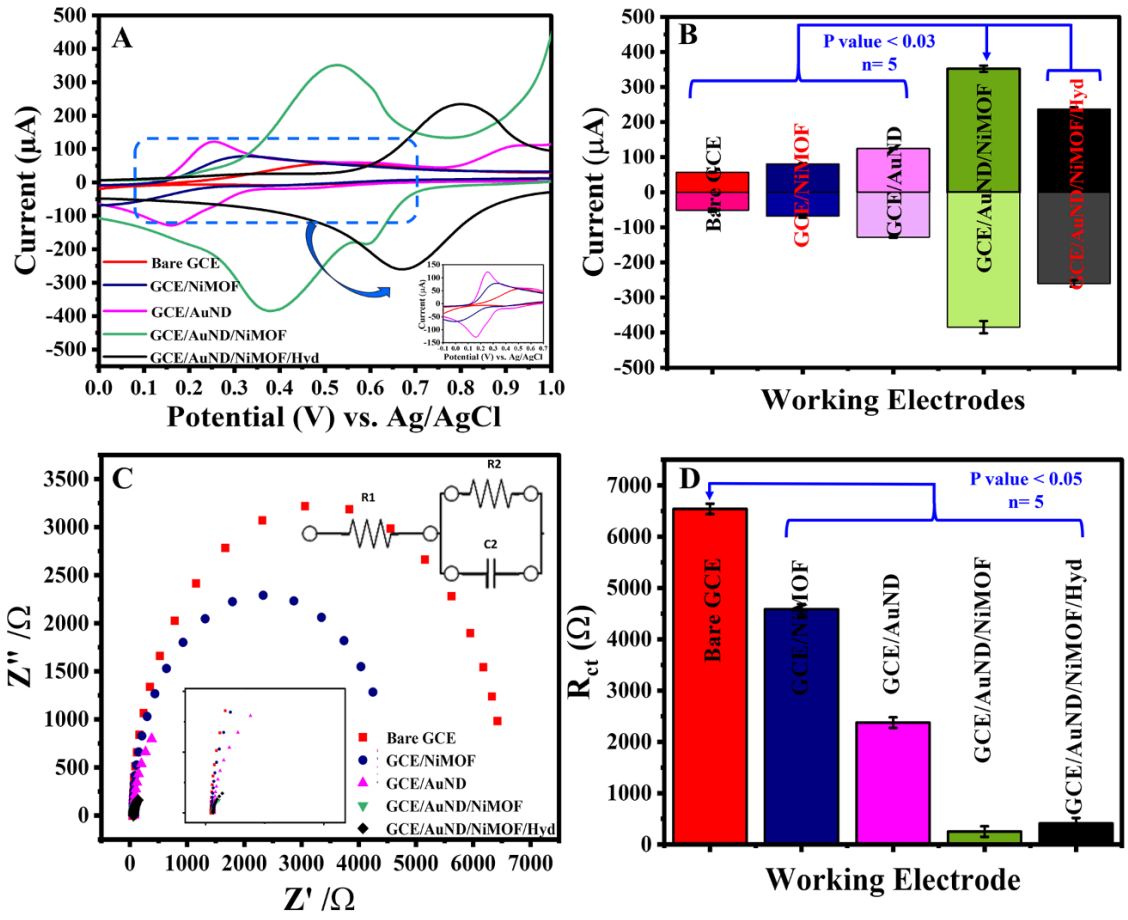

Figure 2.10. ***(A)*** *CV response of bare GCE* ***(red curve)****, GCE/Ni-MOF* ***(blue curve)****, GCE/AuND* ***(pink curve),*** *GCE/Ni-MOF/AuND* ***(green curve),*** *and GCE/Ni-MOF/AuND/Hyd* ***(black curve)*** *surfaces in ZS (5mM; pH-7, scan rate- 50 mV/s);* ***(B)*** *A comparative histogram displays the anodic and cathodic current responses corresponding to each surface, with an amplified response for GCE/AuND/Ni-MOF surface.* ***(C)*** *EIS response in form of Nyquist plots for bare GCE (****red curve****), GCE/Ni-MOF (****blue curve****), GCE/AuND (****pink curve****), GCE/Ni-MOF/AuND (****green curve****), and GCE/Ni-MOF/AuND/Hyd (****black curve****) surfaces in ZS (5mM; pH-7, scan rate- 50 mV/s) with its equivalent circuit model;* ***(D)*** *A comparative histogram displays the Rct values of each surface, with the least resistance for the final surface.*

To further investigate the electrode behavior, stability and migration of ions at the surface of GCE/AuND/Ni-MOF and GCE/AuND/Ni-MOF/Hyd nanohybrid sensing probe, CV experiments were conducted in 5 mM ZS solution by varying scan rates between 10-100 mV s^{-1} [**Figure 2.11 (A and B)**]**.** The developed interface draws attention towards its high stability and diffusion-controlled charge transfer behaviour at elevated potentials. The square root of the scan rates was found to be linearly proportionate to the cathodic (Ipc) and anodic (Ipa) peak currents having a correlation coefficient of 0.99 **(insets of figures)**.

The great charge conducting capabilities of the nanoimprinted probe illuminates its enormous possibility in futures sensing applications.

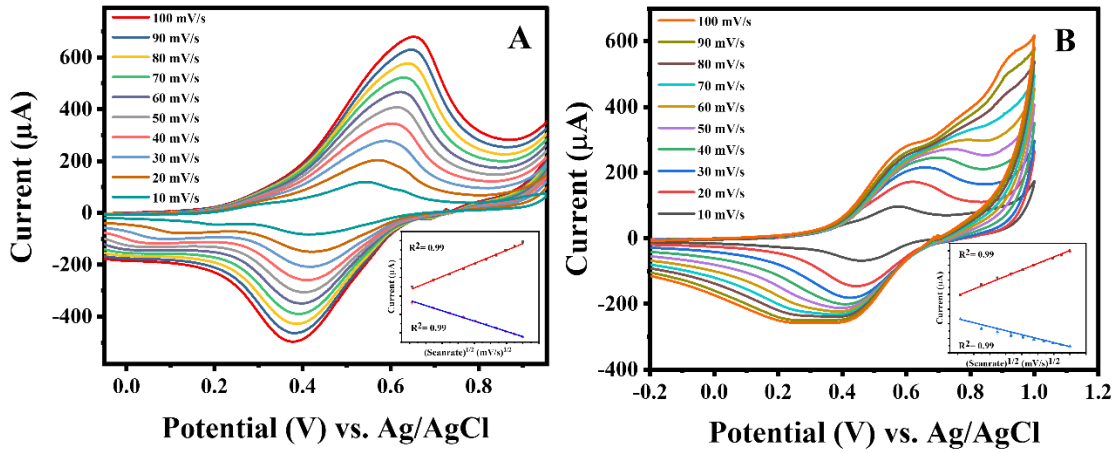

Figure 2.11. ***(A)*** *Scan rate analysis of the GCE/Ni-MOF/AuND probe in ZS (5mM; pH-7) with scan rate varying between 10 to 100 mV/s to evaluate the stability and charge transfer behaviour at the probe surface; inset corresponding to current at different scan rate showed linearity with a correlation coefficient of 0.99, indicating a diffusion-controlled charge transfer behaviour of final interface;* ***(B)*** *Scan rate analysis of the GCE/Ni-MOF/AuND/Hyd probe in ZS (5mM; pH-7) with scan rate varying between 10 to 100 mV/s to evaluate the stability and charge transfer behaviour at the probe surface; inset shows corresponding current at various scan rates demonstrated linearity with a correlation coefficient of 0.99, indicating a diffusion-controlled charge transfer behaviour of the final probe.*

3.2. Analytical performance of GCE/AuND/Ni-MOF/Hyd nanohybrid sensing probe

A set of comparative and control experiments were conducted to undermine the role of each layer viz. bare GCE, GCE/AuND, GCE/AuND/Ni-MOF and GCE/AuND/Ni-MOF/Hyd. The obtained results can be seen through the generated data below. The data was generated for all layers against 0.1 M H_2O_2 concentration (**Figure 2.12 A-B**) to deduce the importance of the constituting matrix material and avoid any misleading interpretations. The bare GCE and GCE/Ni-MOF do not produce any signal response when tested against H_2O_2. However, there was an increment in current magnitude in the case of GCE/AuND. On combining both the layers, which was the case for GCE/AuND/Ni-MOF, a multi-fold increase in the conductivity as well as surface area was observed (as discussed in **Section 3.1.5)**. An increment in the current response than that in GCE/AuND scenario is also observed. This could be due to activation of the Ni

catalytic center when it comes in contact with the Au center of the AuND causing a signal amplification[40]. Then, when the electrocatalytic layer of hydrazine was introduced on this highly conductive surface the enhancement in current response was observed (**purple curve**).

Therefore, this multilayered engineered nanohybrid sensor probe brings out the inherent characteristics of each metal center for deployment in H_2O_2 sensing application which may lead to ultrasensitive detection.

The efficacy of the electrochemically developed nanohybrid sensing probe, GCE/AuND/Ni-MOF/Hyd was analysed for its application by utilizing H_2O_2 as a test molecule. The GCE/AuND/Ni-MOF/Hyd nanohybrid sensing probe was subjected to a series of control experiments to establish that the increment in current magnitude with increase in potential was a resultant of direct and precise electron transfer with H_2O_2. In the first control experiment, a study was conducted at relatively higher concentrations of H_2O_2 i.e., in 0.1 M to 0.5 M H_2O_2**.** In case of the blank reading, no peaks were seen, however, subsequently, current rose with increasing H_2O_2 concentrations between 0.1 to 0.5 M **(Figure 2.12 C).** The curve shows a linear trend signifying concentration dependent signal, with a correlation coefficient of 0.99 **(Figure 2.12 D)**. The regression equation obtained from curve is as follows: $\Delta I\ (\mu A) = 47.131\ (\pm\ 62.626) + 4471.105480\ (\pm 147.5500) \times$ Conc. [H_2O_2 (M)].

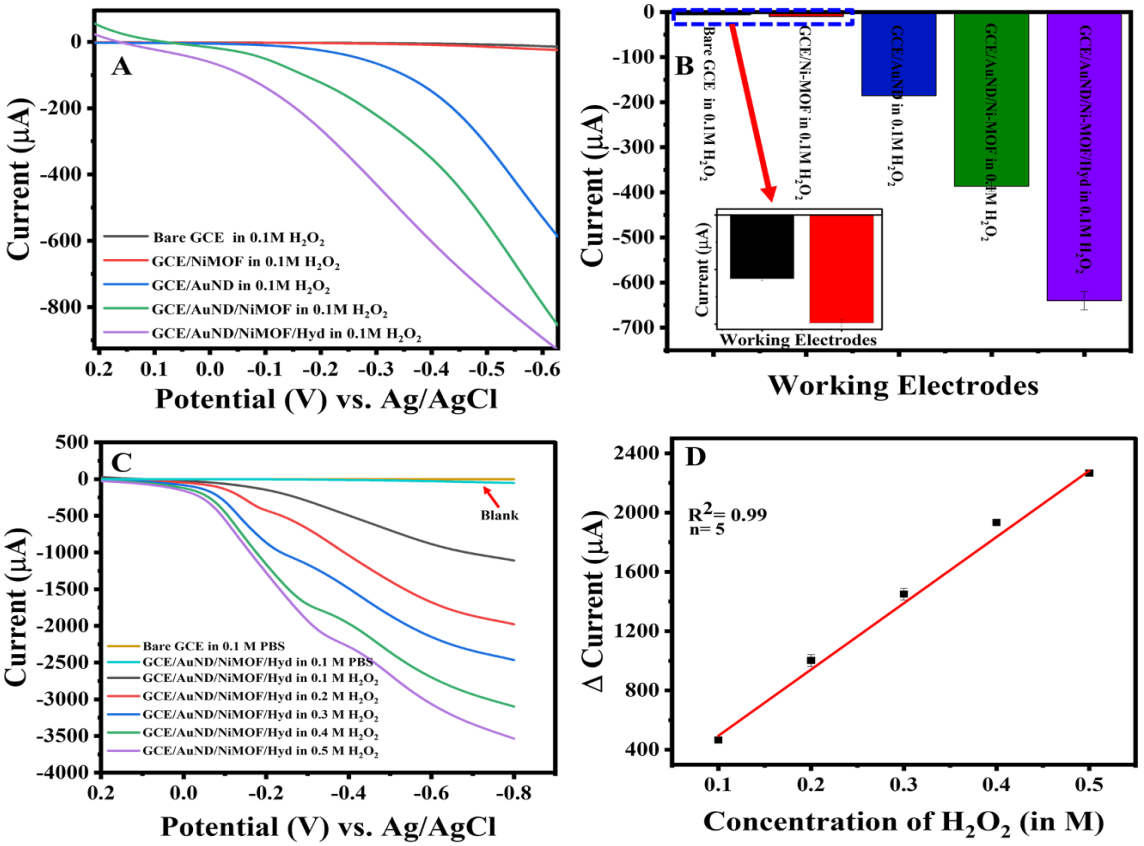

Figure 2.12. ***(A)*** *A comparative LSV curve corresponding to each layer of GCE/AuND/Ni-MOF/Hyd fabrication in PBS and 0.1 M H_2O_2 dissolved in PBS.* ***(B)*** *Corresponding histogram generated from the layer-by-layer study, plotting the cathodic current response generated by the LSV curve measurements.* ***(C)*** *Concentration-dependent control analysis of GCE/AuND/Ni-MOF/Hyd probe in PBS* ***(cyan curve)****, and in 0.1 M* ***(black curve)****, 0.2 M* ***(red curve)*** *and 0.3 M* ***(blue curve),*** *0.4 M* ***(green curve)*** *and 0.5 M* ***(purple curve)*** *H_2O_2 to validate that peak is exclusively due to H_2O_2;* ***(D)*** *Corresponding calibration curve at varying concentrations ranging from 0.1 M to 0.5 M H_2O_2 in PBS with correlation coefficients of 0.99.*

In the second control test, the charge transfer behaviour and stability of the analyte towards the GCE/AuND/Ni-MOF/Hyd probe was analysed. It comprised of scan rate dependent study through an alteration in the scan rates between 10 and 100 mV/s in the presence of 0.1M H_2O_2 **(Figure 2.13A)**. With an increment in scan rates, the cathodic peak currents also increased linearly. The engineered nanohybrid probe demonstrates diffusion-control charge transfer behaviour and excellent surface stability as the cathodic peak current was found to be proportional to the square root of scan rate possessing a correlation coefficient of 0.99 **(Figure 2.13B)**. Therefore, both the control studies inferred that the designed GCE/AuND/Ni-MOF/Hyd nanohybrid sensing probe is highly stable and can effectually sense H_2O_2.

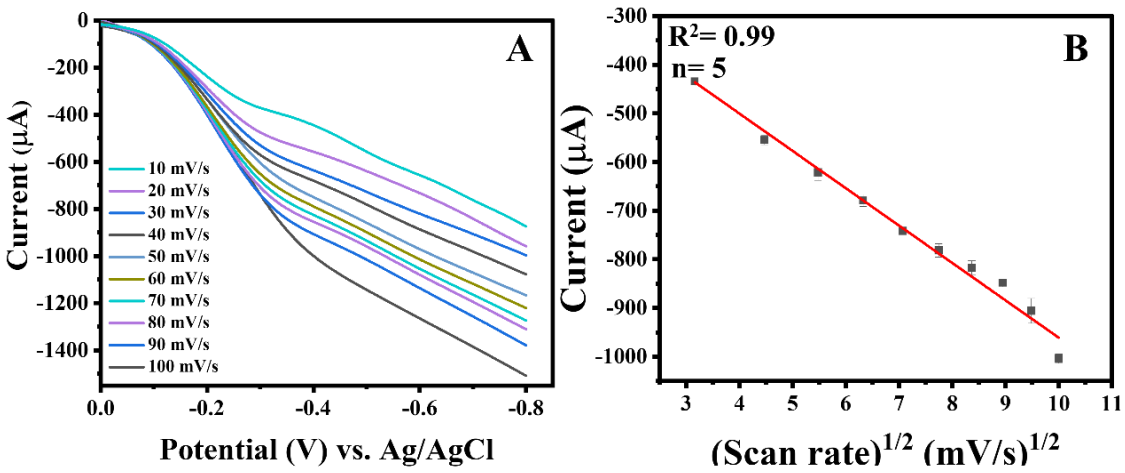

Figure 2.13. ***(A)*** *Scan rate dependent analysis of GCE/AuND/Ni-MOF/Hyd nanohybrid probe in 0.1M H_2O_2 at a scan rate between 10 and 100 mV/s; As scan speeds increased, peak current rose with a small shift to the negative side;* ***(B)*** *corresponding current at different scan rates showed linearity with a correlation coefficient of 0.99.*

The sensing capabilities of the GCE/AuND/Ni-MOF/Hyd nanohybrid probe were further investigated using amperometry to find the minimal concentration since amperometry is considered as a highly sensitive technique[37]. First of all, the signal output for GCE/AuND/Ni-MOF/Hyd (**blank**) was recorded. In this case, a nominal peak at -0.4 V vs. Ag/AgCl was observed **(brown curve)**. Thereafter, the GCE/AuND/Ni-MOF/Hyd probe was evaluated for varying concentrations of H_2O_2 and the signal output was found to be increasing with an increase in H_2O_2 levels **(Figure 2.14A)**. On the basis of the amperometry data, the calibration curve showcased a linearity within the concentration range of 1 x 10^{-8} to 1 x 10^{-15} M **(Figure 2.14B)**. The LOD of H_2O_2 was calculated as 0.34 (±0.05) x 10^{-15} M using **Equation ii**

$$LOD = \frac{3SD_b}{Slope} = \frac{3SD_b}{\frac{dy}{dx}} = \frac{3SD_b}{\frac{dy}{dlnx}\times\frac{dlnx}{dx}} = \frac{3SD_b}{\frac{dy}{2.303(dlogx)}\times\frac{1}{x}} = \frac{3\times2.303\times SD_b\times x}{\frac{dy}{dlogx}} =$$

$$\frac{3\times2.303\times SD_b\times x}{Slope\ of\ semilog\ plot} \qquad \textbf{……Equation ii}$$

where σ_b represents the blank sample's standard deviation, and m is the calibration plot's slope

The linear increment in amperometry current responses with rise in H_2O_2 concentrations in between 1 x 10^{-8} to 1 x 10^{-15} M can be summed up through the regression equation shown below**: I (µA) = 7.64 (±0.42) + 0.48 (±0.03) log Conc. [H_2O_2 (M)].**

Response time, which implies to the time essential for the surface to generate a signal response post the injection of the analyte, has a considerable influence on the sensor's efficacy. For examining the same, CA was executed by injecting varying concentrations of H_2O_2 in blank PBS solution. The current peak was measured at a constant potential of -0.4 V vs. Ag/AgCl and response time values were obtained at varying concentrations. **Figure 2.15** depicts the chronoamperometric response on addition of 10^{-9} M H_2O_2 to a stable current **(a)**. After injecting H_2O_2 at point **(b)**, a sharp spike in current due to diffusion **(c)** was noted between 262.63 seconds and 263.86 seconds; it was followed by saturation of current **(d).** Similar experiments were conducted for different H_2O_2 concentrations, viz. 10^{-10} M, 10^{-12} M, 10^{-13} M, as mentioned in **Figure 2.16.** With an increase in the concentrations, a slight increase in the response time of the GCE/AuND/Ni-MOF/Hyd sensor probe was observed, however, was restricted to <8 seconds. The average response time for the probe was found to be 5.02 ± 0.42 seconds indicating the rapid sensing ability of the system.

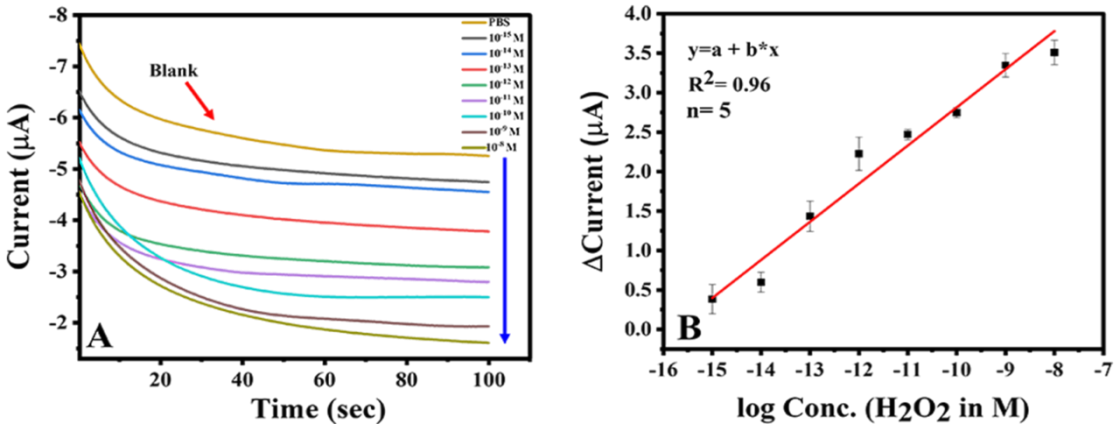

Figure 2.14. ***(A)*** *The chronoamperometric response of GCE/AuND/Ni-MOF/Hyd sensor probe in the range of 1 x 10^{-8} to 1 x 10^{-15} M H_2O_2 in PBS to find the minimal concentration of H_2O_2;* ***(B)*** *Corresponding calibration curve of varying concentrations of H_2O_2 in PBS with a correlation coefficient of 0.96.*

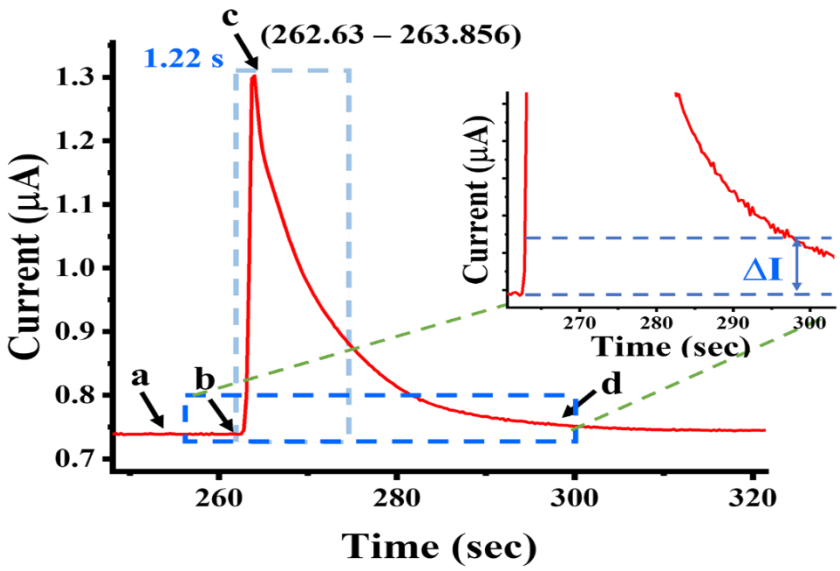

Figure 2.15. *Chronoamperometric evaluation of the GCE/AuND/Ni-MOF/Hyd nanohybrid sensing probe in PBS buffer following injection of 10^{-9}M H_2O_2 concentration showing a response time of 1.22 seconds.* ***(a)*** *stabilized current,* ***(b)****injection point,* ***(c)*** *spike in current, and* ***(d)*** *differential current magnitude post saturation.*

Concentration (in M)	Mean Response Time
10^{-9}	1.5 ± 0.3 sec
10^{-10}	3.3 sec
10^{-12}	7.5 sec
10^{-13}	7.8 sec
Average response time	**5.02 ± 0.42 sec**

Figure 2.16. *Response time of the developed nanosensor probe corresponding to different concentrations of H_2O_2.The mean response time was found to be 5.02±0.42 seconds*

The produced 3D nanohybrid sensitive platform is fascinating because of its short fabrication duration devoid of bulky and conventional synthetic chemical processes, a lower LOD, and faster response time. Additionally, the thorough evaluation of the sensor's analytical performance has been compared to recently published articles on MOF-based H_2O_2 sensors in **Table 2.1**. It is interesting to note that our developed sensor possesses almost 9 times better LOD than few of the recently reported MOF-based sensing setups[41,42]. Not only this, our developed probe is working optimally in the prescribed clinical ranges[24].

Table 2.1. *A comparative analysis of recently published reports on MOF-based sensor.*

S.No.	Probe Composite	Fabrication strategy	Technique used	Reaction time	LOD	LDR	Real Sample	Reference
1.	PA-Tb-Cu MOF	The single material nanoparticle was synthesized by exploring the luminescent behaviour of Tb^{3+}, catalytic potential of Cu^{2+} and using m-phthalic acid(PA) as the ligand moiety.	Fluorescence	20 minutes	0.2 µM	0 to 500 µM	Milk samples	Qi et al.[43]
2.	Fe-MOF	GCE surface was used the working electrode for the one-step electrodeposition of the MOF film using a precursor solution comprising of metal salt and linker molecule dispersed in a probase in DMF.	LSV	N.R.	N.R.	N.R.	N.R.	Zhang et al.[44]
3.	Co-MOF	The MOF/titanium mesh hybrid was synthesized hydrothermally in DMF solvent system at 125 °C for 12 hours by dipping Ti mesh into the reaction chamber. The synthesized entrapped MOF in Ti mesh was used as the WE.	CV	3 seconds	0.25 µM	1 to 13,000 µM	A549 cells	Xia et al.[45]
4.	SWNT-MOF(Cu)	A catalytic ink was dip-coated onto the surface of a gold wire which enabled the growth of the nanotube. It was further modified with SWNTs deposited through the process of CVD. Then, *in situ* synthesized Cu MOF was electrodeposited to obtain the probe surface.	CV, EIS, CA	50 seconds	0.21 µM	1 to 2000 µM	Live cells (RAW 264.7), Raw milk	Nandhini et al.[41]
5.	Ce-UiO-66-BPDC	The probe was prepared using Ce-UiO-66-BPDC functionalized with Au-Pt NPs through the process of electrodeposition.	CV, CA	8 seconds	89 nM	0.15 to 64.8 and 114.8 to 1164.8 µM	A549 cancer cells	Yang et al.[46]
6.	IrNCs@Ti-MOF	Chromogenic reaction was recorded for IrNCs@Ti-MOF, TMB sequentially tested against varying concentrations of H_2O_2 in a sodium acetate–acetic acid buffer.	Colorimetry	2-10 seconds	14.12 µM	0 to 900 µM	Rabbit serum	Mu et al.[47]
7.	M-PCN-222 where, M = Mn, Fe, Co, and Ni	MOFs were synthesized through a microwave-assisted hydrothermal route which displayed a peroxidase-mimic module. Presence of Fe-PCN-222, H_2O_2, and TMB, caused the conversion of TMB into blue-colored ox-TMB.	Colorimetry	10 minutes	Fe-PCN-222: 0.3 µM Mn-PCN-222: 0.9 µM Co-PCN-222: 1.0mM Ni-PCN-222: 9.6 µM	Fe-PCN-222: 1 to 100 mM	Milk, Orange juice, Grape juice, human tears	Shu et al.[48]
8.	Cyclodextrin MOF (CD-MOF)	Peroxidase (POD) and oxidase (OXD)-like mimicking properties were seen in the synthesized MOF. The POD-like activity was seen through TMB as POD substrate which	Fluorescence, Colorimetry	30 minutes	0.06 mM	0.11 to 0.95 mM	HepG2 cells	Tan et al.[49]

		exhibited visible colour change readout. The OXD-like activity was determined using the TMB colorimetry as well as a L-ascorbic acid assay.						
9.	Cu MOF	Polished GCE surface was dipcoated with a mixture of MOF and MWCNTs topped with nafion to obtain the desired electrode.	LSV	N.R.	0.46 µM	3 to 70 µM and 70 to 30000 µM	River water, tap water samples	Zhou et al. [50]
10.	Cu-porphyrin MOF	Polished GCE surface was dropcasted with AgNPs/ Cu-TCPP nanocomposite to obtain the final sensing probe	CV, Amperometry	N.R.	1.2 µM	3.7 µM to 5.8 mM	Disinfectant sample	Ma et al.[51]
11.	Cu MOF	Polished GCE surface was dropped with carboxylated graphene. It was then dipped into the crystalline solution of Cu-MOF precursors to coat the surface with the MOF over 7 hours at RT.	CV, Amperometry	N.R.	6.7×10^{-8} M	2.00×10^{-7} to 1.85×10^{-4} M	Disinfectant sample	Zhou et al.[52]
12.	AuNPs-NH_2/Cu-MOF	Polished GCE surface was dropcasted with AuNPs-NH_2/Cu-MOF suspension to obtain the desired probe.	Amperometry	2 seconds	1.2 µM	5 to 850 µM	HeLa cells	Dang et al.[53]
13.	Cr-MOF	Polished GCE surface was dropcasted with an aqueous suspension of MIL-53-Cr MOF. Nafion and ethanol.	CV	N.R.	3.52 µM	25 to 500 µM	Human serum	Lopa et al.[54]
14.	Ni-MOF	NiO microspheres on titanium carbide was obtained by calcination of Ni-MOF. It was made into solution of ethanol and was dropcasted on GCE surface.	DPV	N.R.	0.34 µM	10 µM to 4.5 mM	N.R.	Ramachandran et al. [23]
15.	Cu-BTC MOF	ITO was chosen as the WE and was dropcasted with Cu-MOF/GO dispersed in aqueous gelatin. Then, the GO was electrochemically reduced to obtain Cu-MOF/ERGOn/ITO	Amperometry	N.R.	0.44 µM	4 µM to 17.334 mM	Milk	Golsheikh et al.[20]
16.	Ni-MOF	Adipic acid based Ni-MOF was mixed with graphite powder. This was packed into a syringe to form the AP-Ni-MOF/CP working electrode.	Amperometry	15 seconds	0.0009 mM	0.004 mM to 60 mM	Lens cleaning solution	Sherino et al.[55]
17.	ZIF-8	Carbon sheet based nanozyme was synthesized using ZIF as template through thermal and sonochemical methods.	Amperometry	N.R.	0.76 µM	1 µM to 20 m	HeLa cells	Wang et al. [42]
18.	***Ni-MOF***	***Imidazole based Ni-MOF was electrodeposited on GCE surface electrocoated with Au nanodendrites. Hydrazine was drop-casted on the final nanohybrid surface to enhance electrocatalysis.***	***Amperometry***	***5.02 ± 0.42 seconds***	***0.34 (±0.13) x 10^{-15} M***	***1 x 10^{-8} to 1 x 10^{-15} M***	***Serum***	***Current Work***

3.3. Selectivity assay

The commercial applications of the developed GCE/AuND/Ni-MOF/Hyd nanohybrid probe requires proving its selectivity towards the specific target analyte present amongst many co-existing interferant molecules within a complex matrix. Therefore, we chose various co-existing molecules such as superoxide free radicals, ascorbic acid, alanine, citric acid, cysteine, glucose along with our target analyte H_2O_2, to examine nanohybrid sensing probe's selectivity. **Figure 2.17A** highlights the signal response of the co-existing molecules which displayed minimal signals at around -0.4 V vs. Ag/AgCl. **Equation iii** was used to determine the coefficient of selectivity (K_{sel}) of the co-existing molecules, with their respective values stated in **Table 2.2**. The values were found to be significantly low ($K_{sel.}$ <<1), with p-value <0.02 emphasizing good selectivity of the developed GCE/AuND/Ni-MOF/Hyd probe for H_2O_2 analysis.

$$K_{sel.} = (Signal)_{Interfering\ molecules} / (Signal)_{H2O2} \quad \textit{...Equation iii}$$

where $K_{sel.}$ denotes the coefficient of selectivity, $(Signal)_{interfering\ molecules}$ are the current corresponding to interferants, and $(Signal)_{H2O2}$ is the response generated by the nanoprobe after being treated with H_2O_2.

Table 2.2. *Coefficient of selectivity (K_{sel}) of the co-existing interferant molecules*

Co-existing molecules	Current Signal (μA)	$K_{sel.}$
Ascorbic Acid	*0.125*	*0.19*
Alanine	*0.010*	*0.015*
Cysteine	*0.012*	*0.018*
Citric Acid	*0.084*	*0.132*
Glucose	*0.009*	*0.014*
Superoxide free radical	*0.016*	*0.025*
H_2O_2	*0.633*	*1*

No significant response was recorded for the co-existing interferants in our experiments due to the electrochemical passivity of developed GCE/AuND/Ni-MOF/Hyd nanohybrid

probe towards these molecules. Another reason could be the analytical potential range, which forbidden other electroactive species from experiencing the redox reaction. Further H_2O_2 was measured using the GCE/AuND/Ni-MOF/Hyd probe in synthetic serum samples in order to evaluate the practicability of our developed sensing matrix.

3.4. Real sample analysis

H_2O_2, an important intermediate in various biological pathways rises in various pathophysiological conditions including cancers. It's excessive concentration in bodily fluids can be a threat to the cellular system which can lead to DNA damage[24]. The GCE/AuND/Ni-MOF/Hyd sensing matrix was evaluated against H_2O_2 in synthetic serum samples to understand its ability to detect the analyte. Spike and recovery test method was adopted to estimate H_2O_2 in synthetic serum samples for evaluation of the potential of constructed nanohybrid sensing probe. Firstly, synthetic serum was equilibrated in PBS followed by spiking it with various concentrations of H_2O_2. The current response was then documented under the optimized experimental settings. The recovery percentage of H_2O_2 at different concentrations was calculated using **equation iv**, as follows,

$$\textit{\% Recovery} = | [S]_{H2O2} - [B]_{H2O2)} | / [SS]_{H2O2} * 100 \quad \textit{....Equation iv}$$

where, $[S]_{H2O2}$ and $[B]_{H2O2}$ are the analytical response of the GCE/AuND/Ni-MOF/Hyd nanohybrid probe in synthetic serum samples with H_2O_2 spiked and blank samples, respectively; $[SS]_{H2O2}$ corresponds to the response in the standard buffer with same concentration of H_2O_2.

The current output generated for varying concentrations of H_2O_2 in the synthetic serum samples (n=5) has been represented using histograms, as shown in **Figure 2.17B** (**olive green).** There is a linear increment in the current response with rise in H_2O_2 concentrations, where the current recovery for different H_2O_2 concentrations ranges

between 90.20 and 94.14% (RSD <3.8 %), when compared with the standard assay results (**blue histogram**). The mathematical depiction of the linear increment in signal output with increasing H_2O_2 concentrations can be explained through the regression equation as follows: $\Delta I\ (\mu A) = 7.03\ (\pm 0.43) + 0.45\ (\pm 0.03) \log$ Conc. [H_2O_2 (M)]. The sensor efficacy was phenomenal in synthetic serum samples, with a co-relation co-efficient of 0.95. During the analysis, the peak current values in real samples were found to be comparable to the corresponding values in the standard calibration plot. These variations could be a resultant of restrictions in ion mobility and minor handling errors in real sample matrices. Serum also comprises of different constituting components however, they did not hinder with our experimental results, thereby, incurring no contrary effects on the sensing matrix. It is also important to mention that the developed nanohybrid sensing probe can be used to accurately monitor H_2O_2 in a variety of biological matrices as it can detect H_2O_2 at various order of magnitudes. These outcomes comprehensibly stipulate that the proposed peroxidase mimic nanohybrid probe is a robust as well as precise sensing platform for H_2O_2, reminiscing its wide commercial prospects.

3.5. Reproducibility and stability assay

Five different GCE/AuND/Ni-MOF/Hyd electrodes were discretely tested to analyse the electrode-to-electrode reproducibility. Various batches of the sensing electrodes were constructed to measure the current response. Only a slight disparity in the electrode-to-electrode current responses was recorded, with RSD value of about <4.5%. Other test conditions and handling errors could be the suggestive reasons for these minor deviations in the output current. The examination of a single nanohybrid nanoprobe against H_2O_2 was also done for multiple iterations (n=5) in succession without any pre-treatment, and the RSD was found to be <3.7%**.** The stability of the nanohybrid architecture without involving any biorecognition elements (antibodies, enzymes, aptamers, etc.) during its

fabrication imparted the GCE/AuND/Ni-MOF/Hyd sensing probe with good stability and reproducibility (**Figure 2.18)**. Periodical assessment of the sensor for five weeks was done to conclude its long-term stability using CA. The current response was recorded at an interval of two-weeks, and the signal was retained up to 95-98% till four weeks. Hence, these results demonstrate nanohybrid sensor probe's reliability and high reproducibility, which are crucial factors governing its shelf life, preservation, and transportation.

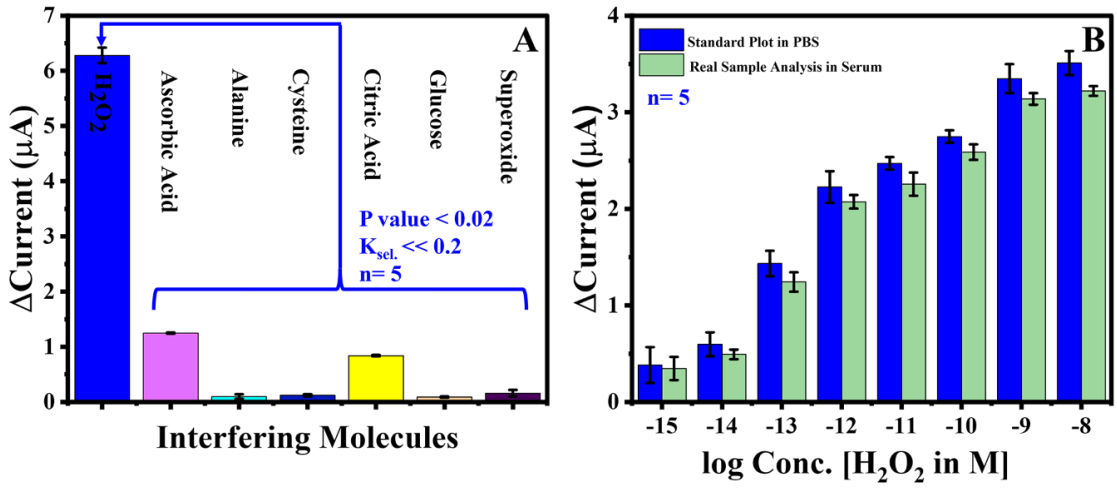

Figure 2.17. ***(A)*** *Interference analysis of GCE/AuND/Ni-MOF/Hyd nanohybrid sensing probes towards various co-existing molecules and H_2O_2;* ***(B)*** *Real sample testing in serum at varying concentrations of H_2O_2 with recovery percentage varied between 90.20 to 94.14%.*

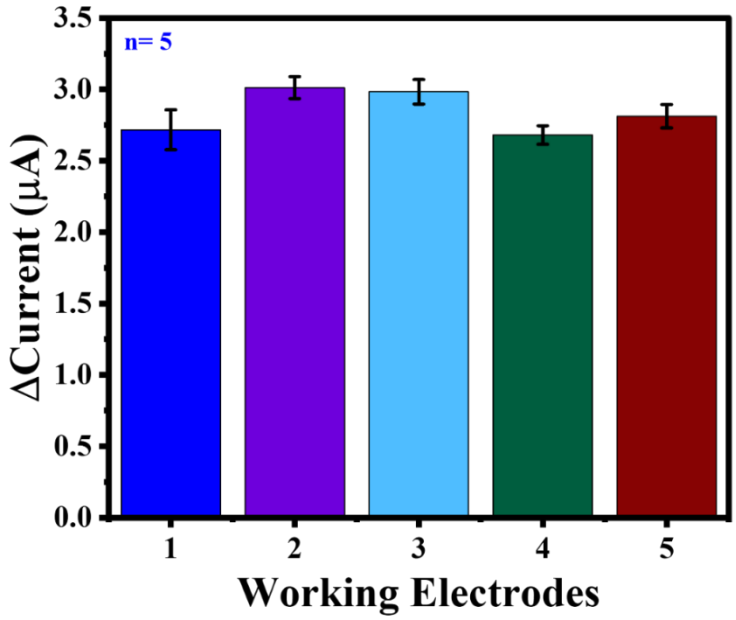

Figure 2.18. *Histogram displaying the electrode-to-electrode reproducibility of GCE/AuND/Ni-MOF/Hyd sensing matrix.*

4. Conclusion

In this work, a novel 3D AuND/Ni-MOF/Hyd nanohybrid sensor surface was developed which was precisely directed towards the non-enzymatic sensing of H_2O_2. The electrodeposition variables were keenly optimized for construction of the matrix with superior analytical performance. The addition of successive layers developed into an interesting hybrid module with enormous surface area and charge transfer characteristics favoring sensing applications. The GCE/AuND/Ni-MOF/Hyd nanohybrid engineered sensing probe was characterized through various physical characterization techniques such as SPM, SEM, EDX, XPS along with a number of electrochemical techniques like, CV, EIS, LSV, and CA. A linear trend in the calibration studies within a H_2O_2 concentration range of 1×10^{-8} and 1×10^{-15} M and a LOD of $0.34 (\pm 0.05) \times 10^{-15}$ M was achieved. The nanohybrid sensing probe displayed a commendable response time of 5.02 ± 0.42 seconds, attributing to its excellent sensitivity towards H_2O_2 determination. When subjected to significant concentrations of interfering species prevalent in the biological microenvironment, it exhibited a high H_2O_2 selectivity with $K_{sel} << 1$. The developed nanohybrid probe could accurately sense H_2O_2 in real sample matrices wherein the outcomes were found to be consistent with the standard conditions. The proposed sensor displays good current recovery percentages and therefore, could be an optimal promising platform for sensitive detection of H_2O_2 in serum samples. To the best of our knowledge, this is the first report of AuND and Ni-MOF nanohybrid structure systematically created by electrodeposition process with remarkable conductivity and catalytic properties. This system could be explored for its future integration with the multiplexing systems for a simultaneous rapid detection of diverse analytes. Such an integrated approach, in our opinion, would be integral for pharmacological analysis prospects and an advantageous module for molecular sensing.

REFERENCES

(1) Cui, Y.; Chen, F.; Yin, X.-B. A Ratiometric Fluorescence Platform Based on Boric-Acid-Functional Eu-MOF for Sensitive Detection of H2O2 and Glucose. *Biosens. Bioelectron.* **2019**, *135*, 208–215. https://doi.org/https://doi.org/10.1016/j.bios.2019.04.008.

(2) Tantawi, O.; Baalbaki, A.; El Asmar, R.; Ghauch, A. A Rapid and Economical Method for the Quantification of Hydrogen Peroxide (H 2 O 2) Using a Modified HPLC Apparatus. *Sci. Total Environ.* **2019**, *654* (2019), 107–117. https://doi.org/10.1016/j.scitotenv.2018.10.372.

(3) Zhang, T.; Huang, C. H. Simultaneous Quantification of Peracetic Acid and Hydrogen Peroxide in Different Water Matrices Using HPLC-UV. *Chemosphere* **2020**, *257*, 127229. https://doi.org/10.1016/j.chemosphere.2020.127229.

(4) Sohrabi, H.; Maleki, F.; Khaaki, P.; Kadhom, M.; Kudaibergenov, N.; Khataee, A. Electrochemical-Based Sensing Platforms for Detection of Glucose and H2O2 by Porous Metal–Organic Frameworks: A Review of Status and Prospects. *Biosensors* **2023**, *13* (3). https://doi.org/10.3390/bios13030347.

(5) Dong, J.; Zheng, J.; Hou, J.; Zhao, P.; Liang, Y.; Lei, J.; Luo, X.; Hou, C.; Huo, D. Au Nanoparticle/CoFc/Metal-Organic Framework as Enzyme-Free Dual-Signal Ratiometric Electrochemical Sensor for In-Situ Determination of Cell-Secreted H2O2. *ACS Appl. Nano Mater.* **2023**, *6* (13), 11630–11639. https://doi.org/10.1021/acsanm.3c01628.

(6) Hira, S. A.; Nallal, M.; Rajendran, K.; Song, S.; Park, S.; Lee, J.-M.; Joo, S. H.; Park, K. H. Ultrasensitive Detection of Hydrogen Peroxide and Dopamine Using Copolymer-Grafted Metal-Organic Framework Based Electrochemical Sensor. *Anal. Chim. Acta* **2020**, *1118*, 26–35. https://doi.org/https://doi.org/10.1016/j.aca.2020.04.043.

(7) Araiso, T.; Tamura, M. Peroxidase. *Tanpakushitsu Kakusan Koso.* **1965**, *32* (6), 895–897. https://doi.org/10.1016/B978-0-12-395630-9.50159-6.

(8) Veitch, N. C. Horseradish Peroxidase: A Modern View of a Classic Enzyme. *Phytochemistry* **2004**, *65* (3), 249–259. https://doi.org/10.1016/J.PHYTOCHEM.2003.10.022.

(9) Xiong, X.; You, C.; Cao, X.; Pang, L.; Kong, R.; Sun, X. Ni2P Nanosheets Array as a Novel Electrochemical Catalyst Electrode for Non-Enzymatic H2O2 Sensing. *Electrochim. Acta* **2017**, *253*, 517–521. https://doi.org/10.1016/J.ELECTACTA.2017.09.104.

(10) Aparicio-Martínez, E.; Ibarra, A.; Estrada-Moreno, I. A.; Osuna, V.; Dominguez, R. B. Flexible Electrochemical Sensor Based on Laser Scribed Graphene/Ag Nanoparticles for Non-Enzymatic Hydrogen Peroxide Detection. *Sensors Actuators B Chem.* **2019**, *301*, 127101.

https://doi.org/10.1016/J.SNB.2019.127101.

(11) Golsheikh, A. M.; Yeap, G. Y.; Yam, F. K.; Lim, H. S. Facile Fabrication and Enhanced Properties of Copper-Based Metal Organic Framework Incorporated with Graphene for Non-Enzymatic Detection of Hydrogen Peroxide. *Synth. Met.* **2020**, *260*, 116272. https://doi.org/10.1016/J.SYNTHMET.2019.116272.

(12) Nandi, I.; Rai, S. K.; Chandra, P. Talanta MOF-Based Nanocomposites as Transduction Matrices for Optical and Electrochemical Sensing. *Talanta* **2024**, *266* (P2), 125124. https://doi.org/10.1016/j.talanta.2023.125124.

(13) Wang, W.; Tang, H.; Wu, Y.; Zhang, Y.; Li, Z. Highly Electrocatalytic Biosensor Based on Hemin@AuNPs/Reduced Graphene Oxide/Chitosan Nanohybrids for Non-Enzymatic Ultrasensitive Detection of Hydrogen Peroxide in Living Cells. *Biosens. Bioelectron.* **2019**, *132*, 217–223. https://doi.org/10.1016/j.bios.2019.02.039.

(14) Murphy, M.; Theyagarajan, K.; Ganesan, P.; Senthilkumar, S.; Thenmozhi, K. Electrochemical Biosensor for the Detection of Hydrogen Peroxide Using Cytochrome c Covalently Immobilized on Carboxyl Functionalized Ionic Liquid/Multiwalled Carbon Nanotube Hybrid. *Appl. Surf. Sci.* **2019**, *492* (March), 718–725. https://doi.org/10.1016/j.apsusc.2019.06.283.

(15) Mani, V.; Govindasamy, M.; Chen, S. M.; Chen, T. W.; Kumar, A. S.; Huang, S. T. Core-Shell Heterostructured Multiwalled Carbon Nanotubes@reduced Graphene Oxide Nanoribbons/Chitosan, a Robust Nanobiocomposite for Enzymatic Biosensing of Hydrogen Peroxide and Nitrite. *Sci. Rep.* **2017**, *7* (1), 1–10. https://doi.org/10.1038/s41598-017-12050-x.

(16) Nandhini, C.; Arul, P.; Huang, S.-T.; Tominaga, M.; Huang, C.-H. Electrochemical Sensing of Dual Biomolecules in Live Cells and Whole Blood Samples: A Flexible Gold Wire-Modified Copper-Organic Framework-Based Hybrid Composite. *Bioelectrochemistry* **2023**, *152*. https://doi.org/10.1016/j.bioelechem.2023.108434.

(17) Purohit, B.; Mahato, K.; Kumar, A.; Chandra, P. Sputtering Enhanced Peroxidase like Activity of a Dendritic Nanochip for Amperometric Determination of Hydrogen Peroxide in Blood Samples. *Microchim. Acta* **2019**, *186* (9), 658. https://doi.org/10.1007/s00604-019-3773-2.

(18) Chen, X.; Chen, X.; Su, B.; Cai, Z.; Oyama, M. PtPd Nanodendrites Supported on Graphene Nanosheets: A Peroxidase-like Catalyst for Colorimetric Detection of H2O2. *Sensors Actuators B Chem.* **2014**, *201*, 286–292. https://doi.org/10.1016/J.SNB.2014.04.067.

(19) Lopa, N. S.; Rahman, M. M.; Ahmed, F.; Chandra Sutradhar, S.; Ryu, T.; Kim, W. A Base-Stable Metal-Organic Framework for Sensitive and Non-Enzymatic Electrochemical Detection of Hydrogen Peroxide. *Electrochim. Acta* **2018**, *274*, 49–56. https://doi.org/10.1016/J.ELECTACTA.2018.03.148.

(20) Golsheikh, A. M.; Yeap, G. Y.; Yam, F. K.; Lim, H. S. Facile Fabrication and Enhanced Properties of Copper-Based Metal Organic Framework Incorporated with Graphene for Non-Enzymatic Detection of Hydrogen Peroxide. *Synth. Met.* **2020**, *260* (December 2019), 116272. https://doi.org/10.1016/j.synthmet.2019.116272.

(21) Xia, L.; Luan, X.; Qu, F.; Lu, L. Co-MOF/Titanium Nanosheet Array: An Excellent Electrocatalyst for Non-Enzymatic Detection of H2O2 Released from Living Cells. *J. Electroanal. Chem.* **2020**, *878*, 114553. https://doi.org/10.1016/J.JELECHEM.2020.114553.

(22) Wang, M. Q.; Zhang, Y.; Bao, S. J.; Yu, Y. N.; Ye, C. Ni(II)-Based Metal-Organic Framework Anchored on Carbon Nanotubes for Highly Sensitive Non-Enzymatic Hydrogen Peroxide Sensing. *Electrochim. Acta* **2016**, *190*, 365–370. https://doi.org/10.1016/J.ELECTACTA.2015.12.199.

(23) Ramachandran, R.; Zhao, C.; Rajkumar, M.; Rajavel, K.; Zhu, P.; Xuan, W.; Xu, Z. X.; Wang, F. Porous Nickel Oxide Microsphere and Ti3C2Tx Hybrid Derived from Metal-Organic Framework for Battery-Type Supercapacitor Electrode and Non-Enzymatic H2O2 Sensor. *Electrochim. Acta* **2019**, *322*, 134771. https://doi.org/10.1016/j.electacta.2019.134771.

(24) Gaikwad, R.; Thangaraj, P. R.; Sen, A. K. Direct and Rapid Measurement of Hydrogen Peroxide in Human Blood Using a Microfluidic Device. *Sci. Rep.* **2021**, *11* (1), 1–10. https://doi.org/10.1038/s41598-021-82623-4.

(25) Xu, T.; Zhang, Y.; Liu, M.; Wang, H.; Ren, J.; Tian, Y.; Liu, X.; Zhou, Y.; Wang, J.; Zhu, W.; Ma, M. In-Situ Two-Step Electrodeposition of α-CD-RGO/Ni-MOF Composite Film for Superior Glucose Sensing. *J. Alloys Compd.* **2022**, *923*, 166418. https://doi.org/10.1016/j.jallcom.2022.166418.

(26) Zhu, Y.; Chandra, P.; Shim, Y. B. Ultrasensitive and Selective Electrochemical Diagnosis of Breast Cancer Based on a Hydrazine-Au Nanoparticle-Aptamer Bioconjugate. *Anal. Chem.* **2013**, *85* (2), 1058–1064. https://doi.org/10.1021/ac302923k.

(27) Shooshtari Gugtapeh, H.; Rezaei, M. One-Step Electrodeposition of a Mesoporous Ni/Co-Imidazole-Based Bimetal-Organic Framework on Pyramid-like NiSb with Abundant Coupling Interfaces as an Ultra-Stable Heterostructural Electrocatalyst for Water Splitting. *ACS Appl. Mater. Interfaces* **2023**, *15* (29), 34682–34697. https://doi.org/10.1021/acsami.3c03021.

(28) Yuan, M.; Wang, R.; Sun, Z.; Lin, L.; Yang, H.; Li, H.; Nan, C.; Sun, G.; Ma, S. Morphology-Controlled Synthesis of Ni-MOFs with Highly Enhanced Electrocatalytic Performance for Urea Oxidation. *Inorg. Chem.* **2019**, *58* (17), 11449–11457. https://doi.org/10.1021/acs.inorgchem.9b01124.

(29) Gougis, M.; Pereira, A.; Ma, D.; Mohamedi, M. Simultaneous Deposition of Cerium Oxide and Gold Nanostructures-Characterization and Analytical

Properties toward Glucose Electro-Oxidation and Sensing. *RSC Adv.* **2014**, *4* (75), 39955–39961. https://doi.org/10.1039/c4ra05374e.

(30) Kitchamsetti, N.; Ramteke, M. S.; Rondiya, S. R.; Mulani, S. R.; Patil, M. S.; Cross, R. W.; Dzade, N. Y.; Devan, R. S. DFT and Experimental Investigations on the Photocatalytic Activities of NiO Nanobelts for Removal of Organic Pollutants. *J. Alloys Compd.* **2021**, *855*, 157337. https://doi.org/10.1016/j.jallcom.2020.157337.

(31) Bagus, P. S.; Nelin, C. J.; Brundle, C. R.; Crist, B. V.; Ilton, E. S.; Lahiri, N.; Rosso, K. M. Main and Satellite Features in the Ni 2p XPS of NiO. *Inorg. Chem.* **2022**, *61* (45), 18077–18094. https://doi.org/10.1021/acs.inorgchem.2c02549.

(32) Huang, H.; Zhao, Y.; Bai, Y.; Li, F.; Zhang, Y.; Chen, Y. Conductive Metal–Organic Frameworks with Extra Metallic Sites as an Efficient Electrocatalyst for the Hydrogen Evolution Reaction. *Adv. Sci.* **2020**, *7* (9), 1–9. https://doi.org/10.1002/advs.202000012.

(33) Kumari, R.; Dkhar, D. S.; Chandra, P. Electrochemically Nanotuned Surface Comprising 3D Bimetallic Dendrites Fabricated on MWCNT for Detection of 1 , 4-Dioxane in Water. *Microchem. J.* **2023**, *191* (April), 108845. https://doi.org/10.1016/j.microc.2023.108845.

(34) Wang, D.; Huang, J.; Liu, Y.; Han, X.; You, T. Facile Synthesis and Electrochemical Properties of Octahedral Gold Nanocrystals. *J. Nanoparticle Res.* **2011**, *13* (1), 157–163. https://doi.org/10.1007/s11051-010-0014-3.

(35) Zeraati, M.; Alizadeh, V.; Kazemzadeh, P.; Safinejad, M.; Kazemian, H. A New Nickel Metal Organic Framework (Ni - MOF) Porous Nanostructure as a Potential Novel Electrochemical Sensor for Detecting Glucose. *J. Porous Mater.* **2022**, *29* (1), 257–267. https://doi.org/10.1007/s10934-021-01164-3.

(36) Allen J. Bard Larry R. Faulkner. *ELECTROCHEMICAL METHODS Fundamentals and Applications Allen*; 2019.

(37) Han, S.; Sun, R.; Zhao, L.; Yan, C.; Chu, H. Molecularly Imprinted Electrochemical Sensor Based on Synergistic Interaction of Honeycomb-like Ni-MOF Decorated with AgNPs and N-GQDs for Ultra-Sensitive Detection of Olaquindox in Animal-Origin Food. *Food Chem.* **2023**, *418* (March), 136001. https://doi.org/10.1016/j.foodchem.2023.136001.

(38) Rodríguez Presa, M. J.; Gassa, L. M.; Azzaroni, O.; Gervasi, C. A. Estimating Diffusion Coefficients of Probe Molecules into Polyelectrolyte Brushes by Electrochemical Impedance Spectroscopy. *Anal. Chem.* **2009**, *81* (19), 7936–7943. https://doi.org/10.1021/ac9009808.

(39) Wang, L.; Bai, J.; Huang, P.; Wang, H.; Zhang, L.; Zhao, Y. Self-Assembly of Gold Nanoparticles for the Voltammetric Sensing of Epinephrine. *Electrochem. commun.* **2006**, *8* (6), 1035–1040. https://doi.org/10.1016/j.elecom.2006.04.012.

(40) Mandal, R.; Baranwal, A.; Srivastava, A.; Chandra, P. Evolving Trends in

Bio/Chemical Sensor Fabrication Incorporating Bimetallic Nanoparticles. *Biosens. Bioelectron.* **2018**, *117* (April), 546–561. https://doi.org/10.1016/j.bios.2018.06.039.

(41) Nandhini, C.; Arul, P.; Huang, S.-T.; Tominaga, M.; Huang, C.-H. Electrochemical Sensing of Dual Biomolecules in Live Cells and Whole Blood Samples: A Flexible Gold Wire-Modified Copper-Organic Framework-Based Hybrid Composite. *Bioelectrochemistry* **2023**, *152*. https://doi.org/10.1016/j.bioelechem.2023.108434.

(42) Wang, X.; Wang, Y.; Liu, Y.; Cao, X.; Zhang, F.; Xia, J.; Wang, Z. MOF-Derived Porous Carbon Nanozyme-Based Flexible Electrochemical Sensing System for in Situ and Real-Time Monitoring of H2O2 Released from Cells. *Talanta* **2024**, *266*, 125132. https://doi.org/10.1016/j.talanta.2023.125132.

(43) Ria, R.; Reale, A.; Vacca, A.; Internal, S. World Journal of Methodology © 2014. **2014**, *4* (2), 73–91.

(44) Zhang, B.; Huang, P.; Chen, J.; Dang, X.; Hu, Y.; Ai, Y.; Zheng, D.; Chen, H. One-Step Controlled Electrodeposition of Iron-Based Binary Metal Organic Nanocomposite. *Appl. Surf. Sci.* **2020**, *504* (October 2019), 144504. https://doi.org/10.1016/j.apsusc.2019.144504.

(45) Xia, L.; Luan, X.; Qu, F.; Lu, L. Co-MOF/Titanium Nanosheet Array: An Excellent Electrocatalyst for Non-Enzymatic Detection of H2O2 Released from Living Cells. *J. Electroanal. Chem.* **2020**, *878*, 114553. https://doi.org/10.1016/j.jelechem.2020.114553.

(46) Yang, H.; Dong, J.; Li, Q.; Wen, L.; Qi, N.; Wang, X.; Xu, F.; Huo, D.; Hou, C. Au and Pt Nanoparticles Grown on Flexible Carbon Fiber Cloth Supports Decorated with Cerium Metal Organic Frameworks for the Real-Time Detection of H2O2in Live Cancer Tissue. *ACS Appl. Nano Mater.* **2022**, *5* (12), 18328–18336. https://doi.org/10.1021/acsanm.2c04176.

(47) Mu, S.; Deng, Y.; Xing, Z.; Rong, X.; He, C.; Cao, S.; Ma, T.; Cheng, C.; Wang, Y. Ir Cluster-Anchored MOFs as Peroxidase-Mimetic Nanoreactors for Diagnosing Hydrogen Peroxide-Related Biomarkers. *ACS Appl. Mater. Interfaces* **2022**, *14* (51), 56635–56643. https://doi.org/10.1021/acsami.2c18676.

(48) Shu, Y.; Ye, Q.; Tan, J.; Lv, H.; Liu, Z.; Mo, Q. Metalloporphyrin-Based Metal-Organic Framework Nanorods for Peroxidase-Like Catalysis. *ACS Appl. Nano Mater.* **2022**, *5* (12), 17909–17918. https://doi.org/10.1021/acsanm.2c03871.

(49) Tan, B.; Zhang, S.; Wang, K.; Yan, Y.; Chu, Z.; Wang, Q.; Li, X.; Zhu, G.; Fan, J.; Zhao, H. Moisture-Resistant and Green Cyclodextrin Metal–Organic Framework Nanozyme Based on Cross-Linkage for Visible Detection of Cellular Hydrogen Peroxide. *Microchim. Acta* **2022**, *189* (8). https://doi.org/10.1007/s00604-022-05389-0.

(50) Zhou, E.; Zhang, Y.; Li, Y.; He, X. Cu(II)-Based MOF Immobilized on

Multiwalled Carbon Nanotubes: Synthesis and Application for Nonenzymatic Detection of Hydrogen Peroxide with High Sensitivity. *Electroanalysis* **2014**, *26* (11), 2526–2533. https://doi.org/10.1002/elan.201400341.

(51) Ma, J.; Bai, W.; Zheng, J. Non-Enzymatic Electrochemical Hydrogen Peroxide Sensing Using a Nanocomposite Prepared from Silver Nanoparticles and Copper (II)-Porphyrin Derived Metal-Organic Framework Nanosheets. *Microchim. Acta* **2019**, *186* (7), 1–8. https://doi.org/10.1007/s00604-019-3551-1.

(52) Zhou, Y.; Li, C.; Hao, Y.; Ye, B.; Xu, M. Oriented Growth of Cross-Linked Metal-Organic Framework Film on Graphene Surface for Non-Enzymatic Electrochemical Sensor of Hydrogen Peroxide in Disinfectant. *Talanta* **2018**, *188* (March), 282–287. https://doi.org/10.1016/j.talanta.2018.05.078.

(53) Dang, W.; Sun, Y.; Jiao, H.; Xu, L.; Lin, M. AuNPs-NH2/Cu-MOF Modified Glassy Carbon Electrode as Enzyme-Free Electrochemical Sensor Detecting H2O2. *J. Electroanal. Chem.* **2020**, *856* (July 2019), 113592. https://doi.org/10.1016/j.jelechem.2019.113592.

(54) Lopa, N. S.; Rahman, M. M.; Ahmed, F.; Chandra Sutradhar, S.; Ryu, T.; Kim, W. A Base-Stable Metal-Organic Framework for Sensitive and Non-Enzymatic Electrochemical Detection of Hydrogen Peroxide. *Electrochim. Acta* **2018**, *274*, 49–56. https://doi.org/10.1016/j.electacta.2018.03.148.

(55) Sherino, B.; Mohamad, S.; Abdul Halim, S. N.; Abdul Manan, N. S. Electrochemical Detection of Hydrogen Peroxide on a New Microporous Ni–Metal Organic Framework Material-Carbon Paste Electrode. *Sensors Actuators, B Chem.* **2018**, *254*, 1148–1156. https://doi.org/10.1016/j.snb.2017.08.002.